Interferon-Induced Transmembrane Protein 3 Blocks Fusion of Diverse Enveloped Viruses by Altering Mechanical Properties of Cell Membranes

Xiangyang Guo, Jan Steinkühler, Mariana Marin, Xiang Li, Wuyuan Lu, Rumiana Dimova, and Gregory B. Melikyan*

ACCESS | Metrics & More | Article Recommendations | Supporting Information

ABSTRACT: Interferon-induced transmembrane protein 3 (IFITM3) potently inhibits entry of diverse enveloped viruses by trapping the viral fusion at a hemifusion stage, but the underlying mechanism remains unclear. Here, we show that recombinant IFITM3 reconstituted into lipid vesicles induces negative membrane curvature and that this effect maps to its small amphipathic helix (AH). We demonstrate that AH (i) partitions into lipid-disordered domains where IAV fusion occurs, (ii) induces negative membrane curvature, and (iii) increases lipid order and membrane stiffness. These effects on membrane properties correlate with the fusion-inhibitory activity, as targeting the ectopically expressed AH peptide to the cytoplasmic leaflet of the cell plasma membrane diminishes IAV−cell surface fusion induced by exposure to acidic pH. Our results thus imply that IFITM3 inhibits the transition from hemifusion to full fusion by imposing an unfavorable membrane curvature and increasing the order and stiffness of the cytoplasmic leaflet of endosomal membranes. Our findings reveal a universal mechanism by which cells block entry of diverse enveloped viruses.

KEYWORDS: IFITM3, viral fusion, hemifusion, amphipathic helix, membrane curvature, membrane rigidity

Infection by enveloped viruses proceeds through fusion of the viral membrane with the target cell membrane. Viral fusion, which is a critical step for establishing infection, is mediated by viral fusion proteins that are transmembrane glycoproteins protruding from the virus envelope. When activated by binding to cellular receptors and/or by acidic pH in endosomes, viral fusion proteins undergo extensive conformational changes.[1] As a result of this refolding, the two contacting membrane leaflets merge to form a hemifusion diaphragm,[2] which allows lipid mixing between the contacting leaflets and ultimately culminates in full fusion through the formation of a fusion pore. Finally, enlargement of a fusion pore allows the release of the viral content into the cytosol and initiates infection.

Interferon-induced transmembrane proteins (IFITMs) are host factors that broadly and potently inhibit infection of diverse enveloped viruses, including the Influenza A virus (IAV), Dengue virus, severe acute respiratory syndrome-associated coronavirus (SARS-CoV), respiratory syncytial virus

(RSV), and Ebola virus (EBOV).[3,4] The IFITM family includes IFITM1, which localizes predominantly at the plasma membrane,[5,6] as well as IFITM2 and IFITM3, which contain an endocytic signal in their cytoplasmic N-terminal domain and are predominantly found in late endosomes and lysosomes.[7,8] IFITM3 alone is responsible for the bulk of antiviral effects of interferon in cell culture[3] and has been shown to be important for restricting viral replication in cell culture and *in vivo*.[9−12]
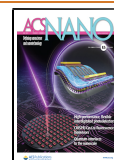
While the importance of IFITM3 in host antiviral defenses *in vitro* and *in vivo* is well-documented, its mechanism of action is not clearly defined. IFITMs are type II transmembrane
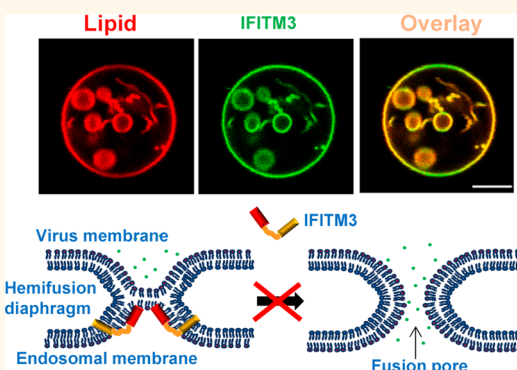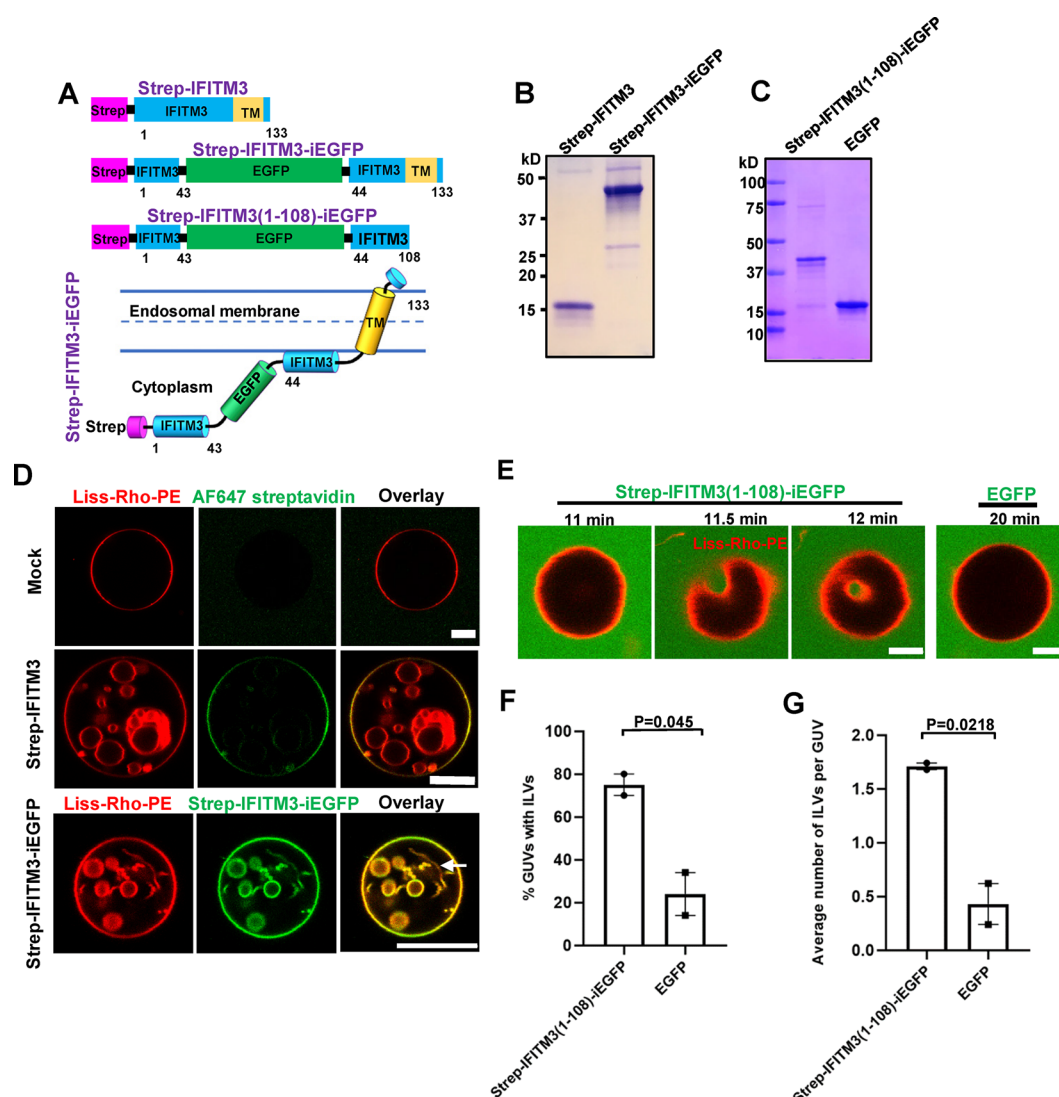
Figure 1. IFITM3 induces negative membrane curvature *in vitro*. (A) Illustration of domains of recombinant IFITM3 with an N-terminal Strep tag (Strep-IFITM3), Strep-tagged IFITM3 with an internal GFP tag (Strep-IFITM3-iEGFP), and C-terminally truncated IFITM3 lacking the transmembrane domain (TM) with a Strep tag and internal GFP tags (Strep-IFITM3(1-108)-iEGFP). Lower cartoon illustrates the membrane topology of Strep-IFITM-iEGFP. The numbers indicate the amino acid numbers. (B, C) SDS-PAGE analysis and Coomassie blue staining of purified IFITM3 recombinant proteins shown in A. (D) Strep-IFITM3- and Strep-IFITM3-iEGFP-reconstituted LUVs (99.0 mol % POPC, 0.5 mol % cholesterol, 0.5 mol % Liss-Rho-PE) or mock-treated LUVs (without protein, top) were dehydrated, electroformed into GUVs, and imaged with a confocal microscope. GUVs prepared from mock-treated LUVs (top) and from Strep-IFITM3-reconstituted LUVs (middle) were stained with Streptavidin AlexaFluor-647. An arrow indicates a nanotube. Scale bars: 10 μm. (E) Time-lapse images of a GUV (99.0 mol % POPC, 0.5 mol % cholesterol, 0.5 mol % Liss-Rho-PE) incubated with 20 μM Strep-IFITM3(1-108)-iEGFP showing an inward budding of the GUV membrane. A control GUV (right) was incubated with 20 μM EGFP and imaged under the same condition. Scale bars: 5 μm. (F) Quantification of IFITM3-induced inward budding plotted as the percentage of GUVs with at least one Strep-IFITM3(1-108)-iEGFP or EGFP-filled intraluminal vesicle (ILV). Data represent mean ± SEM from two independent experiments. Fifty GUVs were analyzed per sample in each experiment. (G) Same as in E, but the plotted values represent the average number of ILVs per GUV. See also Figure S1.

proteins with a cytoplasmic N-terminus, followed by a hydrophobic membrane-associated region and a C-terminal transmembrane domain.[13−15] A number of residues scattered across the cytoplasmic region of IFITM3 have been shown to be essential for antiviral activity.[16] A model for the IFITM3's antiviral activity is through creation of "tough membranes" that are not conducive to fusion, perhaps by altering membrane curvature and fluidity,[16−20] but direct evidence and detailed mechanisms are lacking. Using single virus tracking in live cells, we have previously discovered that IFITM3 traps IAV at a "dead-end" hemifusion stage that does not culminate in full

fusion.[21] In other words, IFITM3 does not restrict the lipid-mixing stage of viral fusion, but rather inhibits the formation of a fusion pore.

There is evidence suggesting that IFITMs may inhibit viral fusion *via* an indirect mechanism that involves recruitment or modulation of other host factors. First, IFITM3 has been reported to bind to and inhibit the function of vesicle-associated membrane protein-associated protein A (VAPA),[8] which disrupts cholesterol transport from late endosomes and causes its accumulation in these compartments. However, high cholesterol content itself does not appear to inhibit virus—

endosome fusion.[18,21−23] Second, it has been proposed that IFITM3 works by recruiting zinc metalloprotease ZMPSTE24 to endosomes and that this effector protein is responsible for virus restriction.[24] However, several lines of evidence support a direct mechanism of IFITM3-mediated virus restriction. We have employed single virus tracking in live cells expressing a functional IFITM3 protein tagged with autofluorescent proteins and shown that IAV enters IFITM3-enriched endosomes, where it undergoes hemifusion, but fails to complete the fusion process.[25] We found that, by contrast, the IFITM3-resistant Lassa virus enters through a distinct pathway that utilizes endosomes devoid of IFITM3. Moreover, IFITM3 incorporation into the viral membrane inhibits fusion mediated by both IFITM3-sensitive and -resistant viral glycoproteins.[25,26] These results suggest that IFITM3 inhibits viral fusion by a proximity-based mechanism that requires the presence of this factor at the sites of viral fusion.

Here, using liposome-based *in vitro* reconstitution assays, we provide evidence that IFITM3 restricts membrane fusion by inducing unfavorable negative curvature and stiffening the cytoplasmic leaflet of a target membrane at the site of viral hemifusion and that these effects map to the small amphipathic helix region of IFITM3.

RESULTS/DISCUSSION

IFITM3 Induces Negative Membrane Curvature *in Vitro*. To understand the molecular mechanism by which IFITM3 inhibits viral fusion, we sought to purify recombinantly expressed IFITM3 and its derivatives, reconstitute these into liposomes, and assess their effects on the properties of lipid bilayers. For the purification purposes, we tagged IFITM3 with an N-terminal Strep-tag (Figure 1A) and verified its antiviral activity by expressing it in HEK 293T cells (Figure S1A) and testing its ability to inhibit IAV infection (Figure S1B). Next, the tagged IFITM3 was expressed in *Escherichia coli*, extracted by Triton X-100, and purified (Figure 1B). In order to visualize the IFITM3 association with membranes, we expressed and purified a fluorescently tagged IFITM3 (referred to as IFITM3-iEGFP, Figure 1A), with EGFP inserted into the N-terminal region of the protein.[25] We have previously shown that IFITM3-iGFP exhibits robust antiviral activity against IAV.[25] The purified proteins were then incorporated into preformed large unilamellar vesicles (LUVs) made of 16:0−18:1 phosphatidylcholine (POPC) and cholesterol, using a detergent-mediated reconstitution protocol.[27] Here, detergent removal from a lipid/protein mixture through hydrophobic adsorption onto Bio-Beads SM-2 triggers protein insertion into lipid bilayers to generate proteoliposomes. Density gradient LUV flotation showed that both IFITM3 and IFITM3-iEGFP were efficiently incorporated into the liposomes (Figure S1C).

We next tested the sidedness of IFITM3 incorporation based upon its accessibility to proteolysis by trypsin. Addition of trypsin to IFITM3- or IFITM3-iEGFP-reconstituted liposomes resulted in a nearly complete cleavage of both molecules, similar to cleavage following proteoliposome solubilization in a detergent (Figure S1D). Thus, both reconstituted proteins appear to insert into liposomes in a preferential orientation, with their large cytoplasmic domains exposed to external medium. This result supports proper reconstitution of IFITM3 proteins in liposomes with an orientation similar to that in endosomal membranes[13,14] (Figure 1A).

In order to assess whether IFITM3 possesses membrane-remodeling activity, IFITM3- or IFITM3-iEGFP-reconstituted proteoliposomes were dehydrated and electroformed into giant unilamellar vesicles (GUVs) using a previously described method.[28] After formation, the N-terminally strep-tagged IFITM3 reconstituted into GUVs could be visualized by staining with the AlexaFlour-647-labeled streptavidin, further supporting its preferential orientation in lipid bilayers (Figure 1D). Importantly, we consistently observed that, in contrast to control GUVs, vesicles containing either IFITM3 or IFITM3-iEGFP protein contained intraluminal vesicles (ILVs) and nanotubes, high curvature structures formed through inward budding of the GUV membrane (Figure 1D and Video 1). The diameter of the nanotubes was below the optical resolution. IFITM3-induced inward budding was confirmed *via* the addition of fluorescein (a small aqueous marker) to the GUV resuspension buffer immediately after electroformation. Fluorescein signal was observed within ILVs of IFITM3-reconstituted GUVs, demonstrating *de novo* inward budding after electroformation, while virtually no vesicles were detected in control GUVs (Figure S1E). Note that some fluorescein-negative ILVs were also observed in IFITM3-reconstituted GUVs, indicating that inward budding occurred during GUV electroformation. The formation of ILVs or tubes from GUVs is a direct visualization of preferred or spontaneous membrane curvature.[29,30] This important finding implies that IFITM3 is capable of inducing negative membrane curvature, *i.e.*, promoting membrane bending away from the protein.[31]

We next asked whether the induction of negative membrane curvature by IFITM3 is mediated by its cytosolic domain (residues 1−108).[14,16] We therefore constructed a soluble IFITM3 fragment with GFP inserted into its N-terminal region (designated IFITM3(1-108)-iEGFP, Figure 1A) and purified it without detergent solubilization (Figure 1C). Interestingly, IFITM3(1-108)-iEGFP showed very weak membrane binding to LUVs (<5% of protein input), as assessed by a liposome co-sedimentation assay[32] (Figure S1F). Next, purified IFITM3(1-108)-iEGFP was added to preformed GUVs containing POPC and cholesterol prepared using a standard electroformation method.[33] IFITM3(1-108)-iEGFP, but not EGFP protein induced inward budding and formation of ILVs within 20 min of addition to GUVs, as illustrated by time-resolved imaging (Figure 1E). As expected, intraluminal vesicles trapped IFITM3(1-108)-iEGFP from the external solution (Figure 1E). Quantification of the inward budding effect of this protein showed that 75% of GUVs treated with IFITM3(1-108)-iEGFP contained ILVs and each GUV contained, on average, 1.7 ILVs (Figure 1F,G). By contrast, EGFP-treated GUVs rarely contained ILVs, and any ILVs detected were not filled with EGFP, suggesting that these structures formed during GUV electroformation. These results imply that the IFITM3 cytosolic domain induces negative membrane curvature, in spite of poor binding to membranes.

IFITM3 Amphipathic Helix Is Responsible for Induction of Negative Membrane Curvature. It has been shown that a highly conserved small region (residues 59−68) of the IFITM3's cytoplasmic domain, predicted to form an amphipathic helix (AH), is essential for antiviral activity.[17,34] Since many amphipathic helices can sense membrane curvature or induce membrane remodeling,[35] we asked whether the AH of IFITM3 is responsible for its ability to induce negative membrane curvature. To answer this question, we made triple alanine substitutions [S61A, N64A, T65A
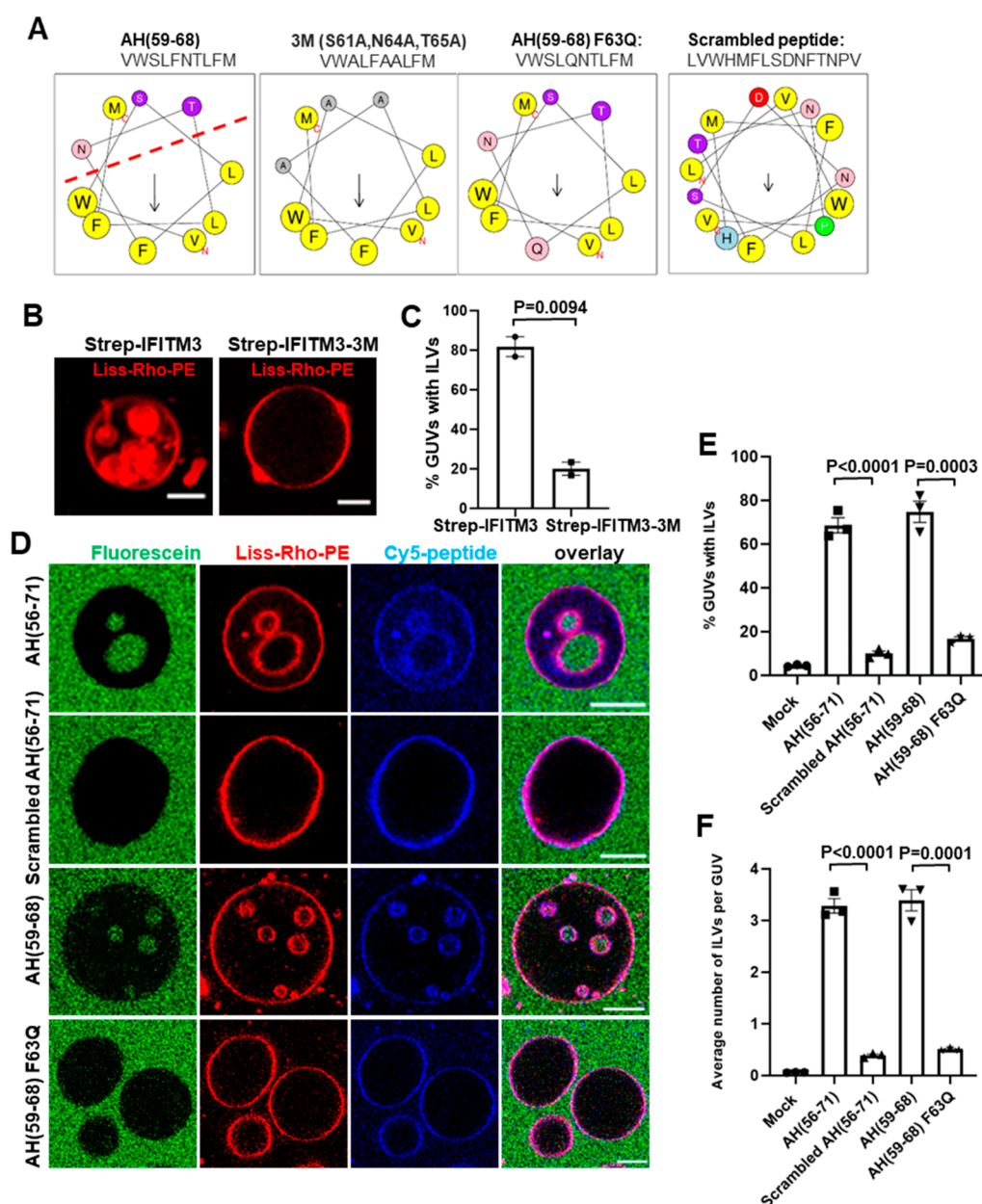
Figure 2. IFITM3 amphipathic helix is responsible for induction of negative membrane curvature. (A) Sequences and helical wheel projection plots created for IFITM3 AH and mutants using HELIQUEST software. Hydrophobic residues are displayed as gray or yellow, while hydrophilic residues are displayed as pink or purple. Arrows represent the magnitude and orientation of the mean hydrophobic moment value calculated by HELIQUEST software. (B) IFITM3- and IFITM3-3M-reconstituted LUVs were dehydrated, electroformed into GUVs, and immediately imaged. Scale bars: 10 μm. (C) Percentage of GUVs, prepared and treated as in B, containing at least one ILV. Data represent mean $\pm$ SEM from two independent experiments; 30 GUVs analyzed per sample in each experiment. (D) GUVs were treated with 10 μM AH(56−71), 10 μM Scrambled AH(56−71), 10 μM AH(59−68), or 30 μM AH(59−68) F63Q for 30 min and imaged. Fluorescein (0.3 μM) was added to the external buffer to mark *bona fide* inward budding of GUVs. Scale bars: 10 μm. (E) Percentage of GUVs, prepared and treated as in D, with at least one ILV containing fluorescein. Mock represents no peptide control that was treated with the same volume of DMSO. Data represent mean $\pm$ SEM of the results of three independent experiments. (F) Same as in E, but plotted values represent the average number of ILVs per GUV. See also Figures S2−S4.

(designated Strep-IFITM3-3M, Figure 2A)] in the AH region, which have been shown to greatly reduce the amphipathic moment of the AH by disrupting the hydrophilic face and abrogate the antiviral activity against IAV.[17] The Strep-IFITM3-3 M mutant was purified and reconstituted into GUVs (Figure S2A). We found that the inward budding activity of the GUV-reconstituted IFITM3-3M was significantly impaired compared to wild-type IFITMs. Only 16.7% of IFITM3-3M-reconstituted GUVs contained at least one ILV,

as compared to 81.7% of wild-type IFITM3-reconstituted GUVs (Figure 2B,C). We also tested the triple alanine mutant in the context of the IFITM3 cytosolic domain tagged with EGFP (IFITM3(1-108)-3M-iEGFP) and found that this soluble construct also exhibited impaired ILV-forming activity when added to preformed GUVs (Figure S2B−E). The above results map the negative curvature-promoting activity of IFITM3 to its AH.
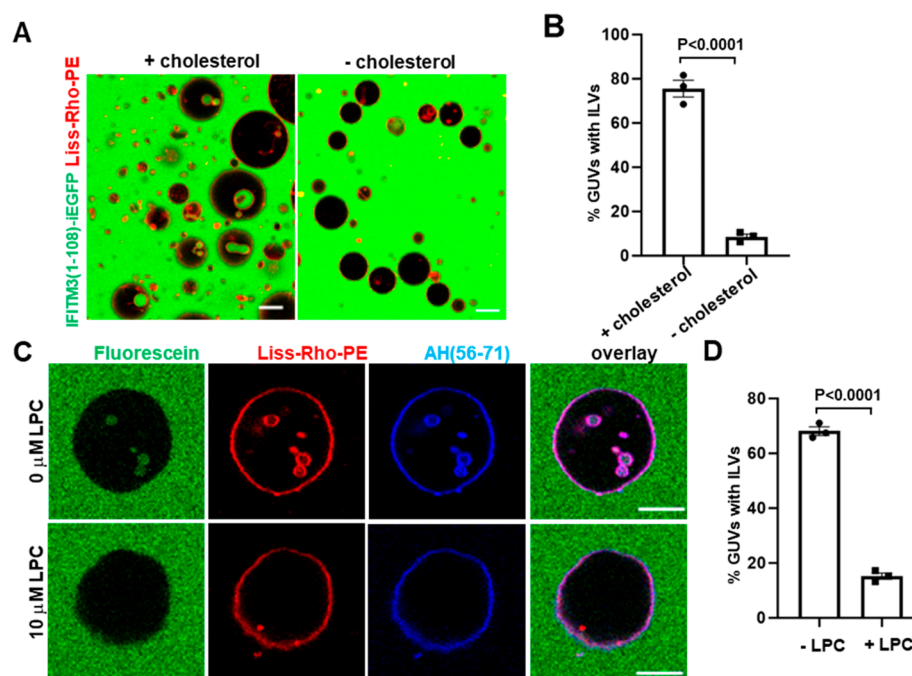
Figure 3. Negative membrane curvature induced by IFITM3 is facilitated by cholesterol and counteracted by lysolipids. (A) GUVs (red channel) with cholesterol (99.0 mol % POPC, 0.5 mol % cholesterol, 0.5 mol % Liss-Rho-PE) or GUVs without cholesterol (99.5 mol % POPC, 0.5 mol % Liss-Rho-PE) were incubated with 20 μM IFITM3(1-108)-iEGFP (green channel) for 30 min and imaged. Scale bars: 20 μm. (B) Quantification of inward budding shows the percentage of GUVs prepared and treated as in A with at least one EGFP-positive intraluminal vesicle (ILV). Data represent mean ± SEM of the results of three independent experiments, with at least 95 GUVs analyzed per sample in each experiment. (C) GUVs (99.0 mol % POPC, 0.5 mol % cholesterol, 0.5 mol % Liss-Rho-PE) were treated with 10 μM AH(56−71) and 10 μM LPC dissolved in methanol (+LPC) or the same volume of methanol (−LPC) for 30 min and imaged. Fluorescein (0.3 μM) was added to mark inward budding of GUVs. Scale bars: 10 μm. (D) Quantification of inward budding showing the percentage of GUVs prepared and treated as in C, with at least one fluorescein-containing ILV. Data represent mean ± SEM of three independent experiments, with at least 35 GUVs analyzed per sample in each experiment. See also Figure S5.

To determine whether IFITM3 AH alone is sufficient to induce negative membrane curvature, a peptide corresponding to this region (residues 59−68) and a longer peptide (residues 56−71) were synthesized and labeled with Cy-5 dye at their N-terminus (Figure 2A). A peptide with a scrambled amino acid sequence (Scrambled AH(56−71)) and the F63Q AH(59−68) mutant peptide (AH(59−68) F63Q) were used as controls. Substitution of the hydrophobic F63 residue to glutamine has been shown to markedly decrease the peptide's amphipathicity by disrupting the hydrophobic face of AH (Figure 2A) and nearly abrogate its antiviral activity.[17] The partition coefficients of the peptides, which reflect their membrane-binding affinity, were measured using a liposome co-sedimentation assay (Figure S3A). The AH(56−71), AH(59−68), and Scrambled AH(56−71) peptides exhibited similar membrane-binding affinities, with more than 80% of the input peptide binding to liposomes (at input peptide to lipid ratio 1:50). The AH(59−68) F63Q exhibited a slightly weaker membrane-binding affinity, with 58.4% of the input peptide binding to liposomes.

Next, membrane-binding and remodeling activity of these peptides added to GUVs were tested by imaging. All peptides were clearly enriched at the GUV membrane (Figure 2D). The peptide to lipid ratio of IFITM3 AH on the GUV membrane was about 1:200, as calculated by comparing the fluorescent intensity of the Cy5-labeled AH peptide with a standard curve generated by analyzing GUVs containing varied concentrations of Cy5-PE (Figure S3B,C). This result is consistent with the membrane partitioning data from the liposome co-sedimenta-

tion assay (Figure S3A). To examine the effect of membrane curvature on the AH binding, we pulled membrane nanotubes from GUVs using a methodology similar to that previously described in ref 36. IFITM3 AH bound similarly to highly positively curved nanotubes and GUVs (Figure S3D). This result implies that the membrane-binding activity of IFITM3 AH is mainly driven by hydrophobic interactions and is rather independent of membrane curvature, implying a homogeneous AH coverage on GUV and ILV membrane segments.

The addition of AH(56−71) or AH(59−68) peptides to preformed GUVs containing POPC and cholesterol led to efficient inward budding, resulting in, respectively, 68.5% and 74.7% of the GUVs containing at least one ILV and, on average, 3.3 and 3.4 ILVs in each GUV (Figure 2D−F). These inner vesicles contained the aqueous marker fluorescein, which was added to GUVs externally, along with the peptides, in order to ensure that ILVs were formed *de novo* through inward budding (Figure 2D). Importantly, addition of the same concentration of the Scrambled AH(56−71) peptide or a 2-fold excess of the AH(59−68) F63Q peptide (to compensate for its slightly lower membrane affinity) did not induce considerable GUV vesiculation, with respectively 9.9% and 16.6% of the GUVs containing, on average, 0.39 and 0.5 ILVs, which was just slightly higher than the basal level of spontaneous ILV formation in control GUVs (Figure 2E,F). A similar effect was observed with GUVs prepared from a natural lipid mixture (liver polar extract) of lipids (Figure S4A). ILVs with optically resolvable diameters, corresponding to low membrane curvature, appear to separate off from the
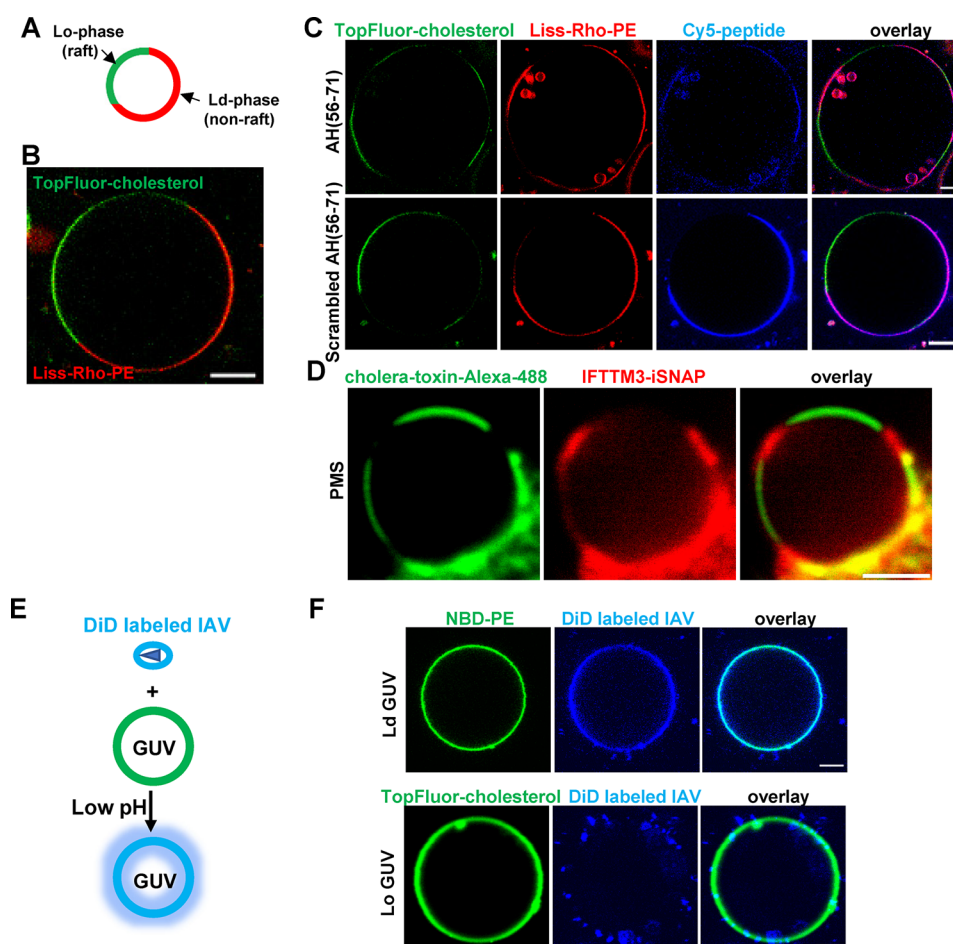
Figure 4. IFITM3 partitions into liquid-disordered membrane domains that support IAV fusion. (A) Diagram of phase-separated GUV. (B) Representative example of phase-separated GUV containing 33.3 mol % DOPC, 33.3 mol % SM, 32.4 mol % cholesterol, 0.5 mol % TopFluor-cholesterol (marker of Lo domain), and 0.5% Liss-Rho-PE (marker of Ld domain). (C) Phase-separated GUVs (33.3 mol % DOPC, 33.3 mol % SM, 32.4 mol % cholesterol, 0.5 mol % TopFluor-cholesterol, and 0.5% Liss-Rho-PE) were incubated with 10 μM Cy5-labeled AH(56−71) or Scrambled AH(56−71) for 30 min and imaged. Scale bars: 10 μm. (D) Plasma membrane spheres were prepared from IFITM3-iSNAP-expressing A549 cells by cell swelling. GM1 was cross-linked with cholera toxin B-AF488 (green) to mark the Lo phase, and SNAP tag was stained with SNAP-cell 647-SIR (red). Scale bar: 2 μm. (E) Diagram depicting lipid mixing between DiD-labeled IAV and GUV triggered by low pH leading to DiD dequenching. (F) Ld GUVs (top, 97.5 mol % DOPC, 2% GM1, 0.5% NBD-PE) or Lo GUVs (bottom, 66.6 mol % SM, 30.9 mol % cholesterol, 2% GM1, 0.5 mol % TopFluor-cholesterol) were mixed with DiD-labeled IAV, lipid mixing was triggered by addition of citrate buffer to achieve the final pH of 5.0, and samples were immediately imaged. Scale bars: 5 μm. See also Figure S6.

outer membrane, as judged by their position in the GUVs. This is indicative of a high spontaneous membrane curvature generation potential of AH, as membrane fission of buds is triggered by mismatch between ILV curvature and membrane spontaneous curvature.[30] Notably, inward-facing nanotubes—high curvature structures that are below the optical resolution—were consistently observed in the lumen of GUVs that were treated with AH peptide, but not in GUVs treated with AH(59−68) F63Q mutant peptide (Figure S4B,C). On the basis of the ability to produce subresolution nanotubes and low peptide/lipid ratio, we estimated the local curvature, sometimes called intrinsic curvature, per peptide density (m_0) generated by IFITM3 AH to be rather high (−6.4 nm^{-1}, see Supporting Appendix). This curvature magnitude is comparable to that of the well-characterized cellular curvature inducing proteins, such as amphiphysin 1.[37] Taken together, these results confirmed that IFITM3 AH alone is sufficient to induce negative membrane curvature and that this effect is critically dependent on the amphipathicity of this region.

Negative Membrane Curvature Induced by IFITM3 Is Facilitated by Cholesterol and Counteracted by Lysolipids. Different lipids have different effective shapes manifested in spontaneous curvature that can impose positive or negative curvature to a lipid bilayer.[38] Lipids are categorized as "cylindrical", "cone", and "inverted cone" shaped. Cylindrical lipids, such as phosphatidylcholine (PC), prefer planar membranes, whereas cone-shaped lipids, such as cholesterol and phosphatidylethanolamine (PE), prefer negative membrane curvature, and inverted cone-shaped lipids, like lyso-PC (LPC), promote positive membrane curvature.[39] Curvature of biological membranes is determined by an interplay between membrane proteins and lipids.[30,40,41]

We therefore tested whether lipids play a role in IFITM3-mediated GUV vesiculation. First, we electroformed POPC GUVs with or without cholesterol (0.5 mol %) and treated these with IFITM3(1-108)-iEGFP. Whereas this treatment resulted in 75.5% of cholesterol-containing GUVs with ILVs, a significant impairment of inward budding (8.5% GUVs with

ILVs) was observed in the absence of cholesterol (Figure 3A,B). Similarly, addition of the AH(56−71) peptide to GUVs without cholesterol also failed to induce efficient inward budding, although the binding of AH(56−71) peptide to GUVs was not affected by the absence of cholesterol (Figure S5A−C). Notably, IFITM3-induced inward budding in GUVs was independent of cholesterol concentration up to 20 mol % (Figure S5D). Importantly, AH(56−71)-mediated inward budding of GUVs without cholesterol could be rescued by inclusion of another conical lipid, DOPE (20 mol %) (Figure S5E). This finding indicates that IFITM3-induced negative membrane curvature is facilitated by cone-shaped lipids.

We next tested the effect of an inverted conical lipid, LPC, on GUV budding mediated by IFITM3. LPC was first titrated by adding to preformed GUVs containing POPC and cholesterol. As expected based upon positive curvature induced by this lipid,[42] we observed outward budding of the GUV membrane in an LPC dose-dependent manner (Figure S5F). A moderate concentration of LPC (10 μM) was then added together with the AH(56−71) peptide to preformed GUVs containing POPC and cholesterol. LPC abolished the AH(56−71)-induced GUV inward budding (Figure 3C,D), showing that negative membrane curvature caused by IFITM3 is counteracted by the presence of an inverted conical lipid in the membrane.

IFITM3 Partitions into Liquid-Disordered Membrane Domains That Support IAV Fusion. Cell membranes contain lipid rafts, which are liquid-ordered domains with more tightly packed lipids than the nonraft, liquid-disordered phase of the bilayer.[43] Lipid rafts form a platform for signaling proteins and receptors and have been suggested to serve as potential virus entry sites,[44] but a formal proof is still lacking due to the fact that small and dynamic lipid microdomains are difficult to visualize in living cells. Post-translational modifications, such as S-palmitoylation, target transmembrane proteins to lipid rafts.[45] Palmitoylation of the conserved cysteine residues downstream of the IFITM3 AH region regulate the membrane domain targeting and antiviral activity of this protein.[46] We therefore asked whether IFITM3 has any preference for lipid microdomains and whether lipid rafts may play a role in IFITM3's antiviral activity. To address this question, we utilized phase-separated GUVs as a model for microdomains within the endosomal membrane.[47] GUVs containing sphingomyelin (SM), cholesterol, and unsaturated phosphatidylcholine (DOPC) segregate into lipid ordered (Lo) and lipid disordered (Ld) phases,[48] corresponding to lipid raft and nonraft microdomains of biological membranes, respectively. Incorporation of fluorescent markers partitioning into Lo (Top-cholesterol) or Ld (Liss-Rho-PE) phases allowed the visualization of the two phases (Figure 4A,B). The AH(56−71) peptide added to phase-separated GUVs partitioned to the Ld phase and caused inward budding from this domain, as evidenced by ILVs containing exclusively the Ld marker Liss-Rho-PE (Figure 4C). The Scrambled AH(56−71) peptide also exhibited an Ld phase preference, but failed to cause inward budding from this phase (Figure 4C). Intriguingly, palmitoylation of Cys71 of a fluorescently tagged AH(56−75) peptide did not target this peptide to the Lo phase. This peptide clearly partitioned to the Ld phase and appeared to concentrate at the phase boundary (Figure S6A).

We then asked whether the full-length IFITM3 protein similarly localizes to the Ld phase in cellular membranes. IFITM3 transits through the plasma membrane en route to endolysosomal compartments and is thus present on the cell surface.[15,49] We used plasma membrane-derived spheres[50] to visualize IFITM3 partitioning into membrane rafts. We expressed IFITM3 with an internal SNAP-tag inserted at the same site as EGFP in IFITM3-iGFP.[25] SNAP-tagged IFITM3 was expressed in A549 cells and specifically labeled with a fluorescent substrate SNAP-Cell 647-SiR. Next, membrane spheres derived from the plasma membrane were obtained by cell swelling, and phase separation within these spheres was induced by cross-linking a lipid raft marker GM1 with a labeled cholera toxin B subunit[50] (Figure 4D). The IFITM3-iSNAP partitioned to the Ld phase of membrane spheres, suggesting that the full-length IFITM3 is also localized to nonraft domains in living cells (Figure 4D).

Next, we sought to investigate the link between the IFITM3 localization to the Ld phase and its antiviral activity. To answer this question, we employed a lipid mixing assay between IAV labeled with a self-quenching concentration of the lipophilic dye DiD and GUVs. Here, addition of labeled IAV to GUVs followed by acidification should trigger lipid mixing, which can be detected by the appearance of dequenched DiD in the GUV membrane (Figure 4E). Using phase-separated GUVs, we found that, upon triggering IAV-GUV fusion by exposure to low pH, DiD accumulated within the Ld domain (Figure S6B). This DiD accumulation occurred in spite of the preference of the IAV receptor ganglioside GM1 for the Lo domain (Figure S6C), suggesting that IAV lipid mixing occurred in a nonraft phase. To test the possibility of DiD redistribution between Lo and Ld phases after viral fusion, single-phase GUVs were prepared. Low pH-induced IAV lipid mixing occurred very efficiently with Ld-phase GUVs (Figure 4F), whereas no lipid mixing was detected between IAV and Lo-phase GUVs, in spite of the efficient binding of labeled viruses to these vesicles (Figure 4F). Taken together, these results imply that IFITM3 concentrates in nonraft domains, which appear to be the sites supporting IAV fusion with synthetic membranes.

IFITM3 Amphipathic Helix Increases Lipid Order and Stiffens Membranes. Since IFITM3 tends to localize to nonraft microdomains of membranes and induces negative curvature through its AH, we asked whether this helical domain affects other membrane properties, such as lipid order and membrane stiffness. Lipid order, which reflects the mobility of hydrocarbon tails of lipids,[51] has been assessed using the lipophilic probe Laurdan. Laurdan is an environment-sensitive dye that intercalates between the hydrocarbon tails of lipids and exhibits a red-shift in the emission spectrum upon exposure to polar solvent, i.e., in lipid disordered domains. The Laurdan emission shift is parametrized by generalized polarization (GP), which is a normalized difference between Laurdan's emission at two wavelengths[52] (Figure S7A). We thus used Laurdan to probe the effect of the IFITM3 AH peptides on LUVs. Addition of either AH(56−71) or AH(59−68) peptide caused a strong positive shift in the Laurdan GP, indicating a marked increase in lipid order (Figure 5A). In contrast, the AH(59−68) F63Q mutant did not have a significant effect on GP, and the Scrambled AH(56−71) peptide only modestly altered GP. A detectable effect of the scrambled peptide on GP is likely due to its higher binding affinity to membranes (Figure 5A). These findings imply that IFITM3 AH specifically increases the lipid order. We then asked whether full-length IFITM3 also increases lipid order. To address this question, we performed Laurdan GP measurements using plasma membrane spheres derived from
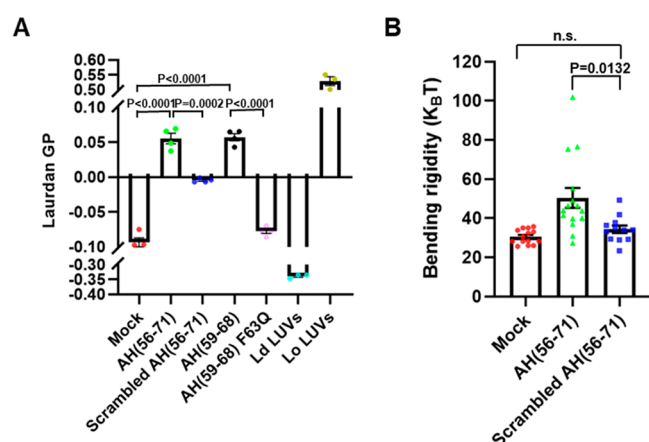
Figure 5. IFITM3 amphipathic helix increases lipid order and stiffens membranes. (A) Membrane binding of IFITM3 AH induces lipid ordering. Two millimoles of LUVs (99.5 mol % POPC, 0.5 mol % cholesterol) was incubated with 25 μM Laurdan in the presence or absence of 40 μM of the indicated IFITM3-derived peptide at 25 °C. Ld LUVs (2 mM, 99.5 mol % POPC, 0.5 mol % cholesterol, 37 °C) and Lo LUVs (66.6 mol % SM, 33.4 mol % cholesterol, 25 °C) were incubated with 25 μM Laurdan without addition of peptide. Laurdan fluorescence was then measured at 440 and 490 nm, and the ratio was used to calculate the general polarization (GP) of Laurdan using the equation GP = $(I_{440} - I_{490})/(I_{440} + I_{490})$. Data represent mean $\pm$ SEM of at least three independent experiments. (B) The membrane bending rigidity increases in the presence of IFITM3 AH peptide. Membrane bending rigidity values were measured by fluctuation analysis of the thermally induced motion of the POPC + cholesterol GUV membrane in 100 mM sucrose/1 mM HEPES at pH 7.4, incubated with DMSO (at a final concentration of ~0.1 v/v%; mock) or with AH(56−71) or Scrambled AH(56−71) in DMSO at a final peptide concentration of 3 nM. Bending rigidity was measured based on the Fourier spectrum of the cross-sectional contour, as obtained from discrete time series of optical snapshots. Data represent mean $\pm$ SEM, and each data point corresponds to an individual vesicle. See also Figure S7.

IFITM3-iSNAP-expressing A549 cells (Figure S7B,C). The presence of IFITM3 in the plasma membrane significantly increased the GP value, suggesting that full-length IFITM3 also increases lipid order.

It has been reported that lipid order correlates with the bending rigidity of cellular membranes.[53] We therefore asked whether IFITM3 AH can affect the membrane's bending rigidity. The membrane bending rigidity was measured by fluctuation analysis of the thermally induced motion of the GUV membrane, as described previously.[54] Addition of AH(56−71) resulted in a significant increase in the bending rigidity of the GUV membrane (Figure 5B). In contrast, the Scrambled AH(56−71) peptide did not have a significant effect on the bending rigidity. These important findings show that IFITM3 AH specifically stiffens lipid membranes and increases the lipid order.

IFITM3 Amphipathic Helix Alone Is Sufficient to Inhibit Membrane Fusion. The ability of IFITM3 AH to induce negative curvature, increase the lipid order, and stiffen the membrane implies that this region is responsible for the protein's inhibitory effect on viral fusion. We hypothesized that AH interaction with the cytoplasmic leaflet of endosomal membranes is necessary and sufficient for the antiviral activity of IFITM3. However, testing this hypothesis *in vitro* using

reconstituted IFITM3 is not feasible. This is because incoming viruses do not come into contact with the N-terminal cytoplasmic region of IFITM3 that encompasses the AH, whereas reconstituted IFITM3 and IFITM3 AH localize to the external leaflet of liposomes (Figures 1A, S1D, and 3D) that comes in contact with exogenously added viruses. To fulfill the topological requirement for virus/IFITM3 positioning across a target membrane, using exogenously added peptides, we resorted to exocytosis (Figure 6A). Secretory vesicle fusion with the plasma membrane affords an easy access to the external (trans) leaflet of a target membrane. We used glucose-stimulated insulin secretion as a model to study the effect of IFITM3 on SNARE-mediated vesicle fusion (Figure 6A). INS-1E cells secrete insulin upon stimulation with high glucose.[55] To increase the sensitivity of detection of secreted insulin, INS-1E cells were transduced with a vector expressing a proinsulin-luciferase fusion protein,[56] which can be detected by luciferase activity following exposure to a high-glucose solution (Figure 6B). When cells were pretreated with AH(59−68), which effectively bound to the plasma membrane (Figure S8A), high-glucose stimulation resulted in significantly reduced insulin secretion. In contrast, the AH(59−68) F63Q peptide had no effect on insulin secretion, even when added in a higher concentration than the wild-type peptide (Figures 7B and S8B). To test whether inhibition of secretion was related to the IFITM3 AH-mediated negative membrane curvature, we pretreated cells with LPC, which induces positive curvature. LPC promoted insulin secretion, in agreement with the previous study[57] (Figure 6C). Importantly, LPC added with IFITM3 AH counteracted the suppression of insulin secretion by this peptide. Taken together, these results imply that IFITM3 AH is sufficient to inhibit membrane fusion and that this inhibition is dependent on its ability to induce negative membrane curvature.

To directly explore the role of IFITM3 AH in the context of viral fusion, we expressed IFITM3 AH with an EGFP tag in cells and targeted it to the cytoplasmic leaflet of the plasma membrane with a CAAX motif[58] (Figure 6D). Interestingly, expression of this construct induced lots of protrusions/filopodia-like structures on the plasma membrane, which were not observed in cells expressing the AH F63Q mutant (Figure S8C). This finding suggests that IFITM3 AH induces negative curvature in cellular membranes. We then attached the influenza A viruses to cells expressing wild-type or mutant AH in the cold and forced viral fusion with the plasma membrane by exposing to a warm acidic buffer. The presence of IFITM3 AH in the cytoplasmic leaflet of the plasma membrane inhibited the forced IAV fusion with the plasma membrane, whereas the F63Q mutant did not exhibit an inhibitory effect (Figure 6 E−G). We also verified the above inhibitory effect of the IFITM3 AH using a direct IAV pseudovirus fusion assay. Similar to the AH effect on IAV infectivity, incorporation of this peptide into the cytoplasmic leaflet of the plasma membrane reduced the efficiency of forced IAV pseudovirus−cell fusion, whereas the F63Q mutant was without effect (Figure S8D). These results support the notion that IFITM3 AH is sufficient to directly inhibit viral fusion.

To further investigate the link between membrane curvature and antiviral activity of IFITM3, we asked whether the IFITM3 AH can be replaced with unrelated amphipathic helixes of other proteins, such as M2 of IAV (M2 AH). The M2 AH has been reported to induce negative curvature and increase lipid order during IAV budding from the plasma
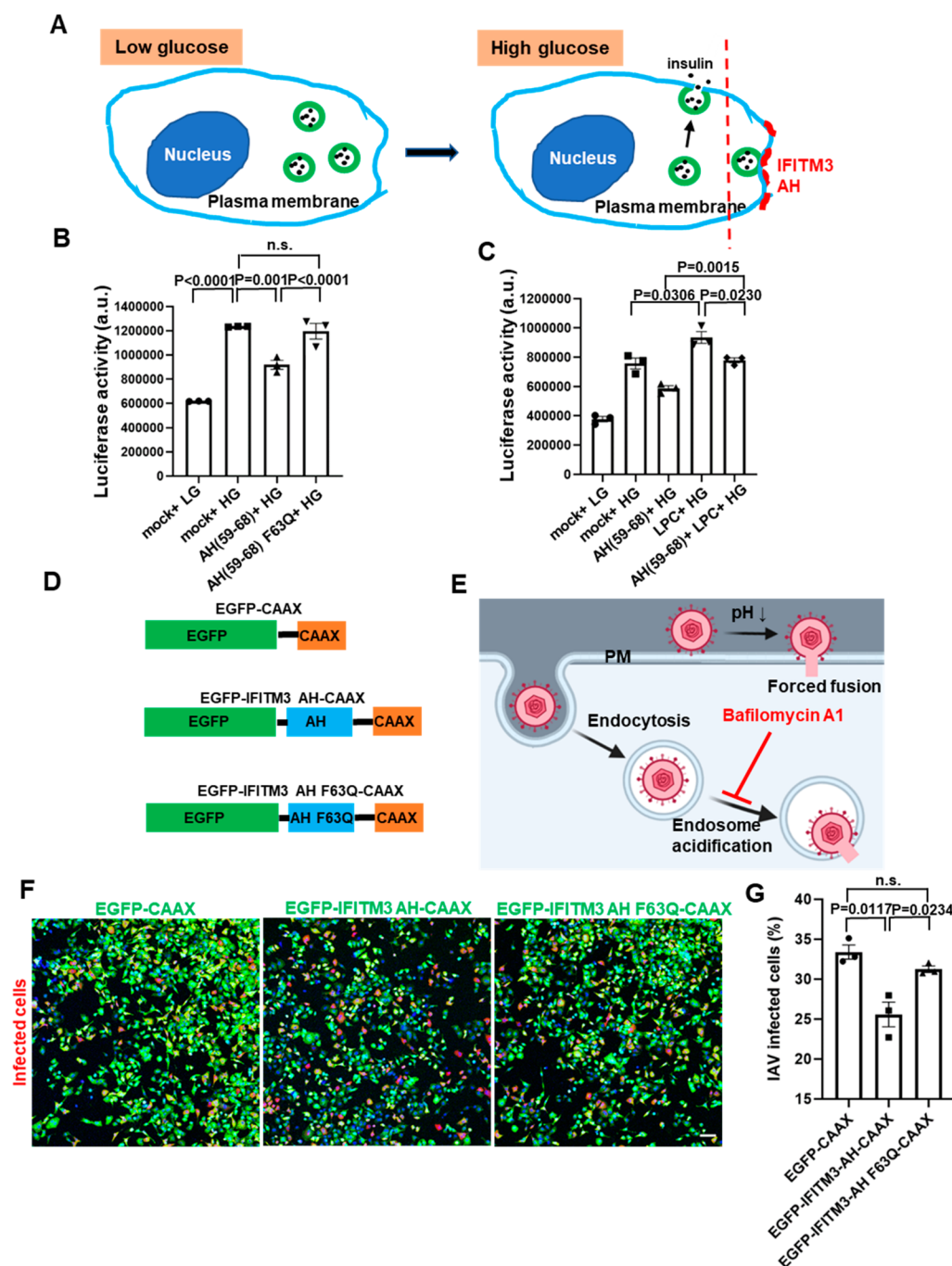
Figure 6. IFITM3 amphipathic helix inhibits membrane fusion. (A) Diagram illustrating glucose-stimulated insulin secretion and its block by IFITM3 AH. (B) IFITM3 AH peptide inhibited glucose-stimulated insulin secretion of INS-1E cells. INS-1E cells transduced with proinsulin-luciferase fusion construct were preincubated for 5 min with 5 μM AH(59−68) or 10 μM AH(59−68) F63Q or the same volume of DMSO (mock) and then stimulated for 20 min with high-glucose (HG, 20 mM) buffer or with low-glucose (LG, 2.8 mM) as control. Luciferase activity was determined by adding the coelenterazine substrate to the supernatant and reading on a luminescence counter. Data represent mean ± SEM of the results of three independent experiments. (C) As in B, but for samples preincubated for 5 min with AH peptide or DMSO supplemented with 20 μM LPC. (D) Illustration of the EGFP-CAAX, EGFP-IFITM3 AH-CAAX, and EGFP-IFITM3 AH F63Q-CAAX chimeras. (E) Diagram illustrating forced IAV fusion with the plasma membrane. IAV entry through endosomal pathway was blocked by incubating the cells with Bafilomycin A1 to inhibit the acidification of endosomes. (F) Forced fusion mCherry-expressing IAV (red) with the plasma membrane of A549 cells expressing EGFP-CAAX, EGFP-IFITM3 AH-CAAX, or EGFP-IFITM3 AH F63Q-CAAX (green) on the cytoplasmic leaflet of the plasma membrane. Nuclei were stained with Hoechst (blue). Scale bar: 100 μm. (G) Quantification of IAV infection shown in F. Infected cells are plotted as percentage of total cells with EGFP fluorescence, while EGFP-negative cells were excluded from analysis. Data represent mean ± SEM of the results of three independent experiments. See also Figure S8.

membrane.[59,60] We thus replaced the IFITM3 AH with M2 AH in the context of an mTFP1-tagged protein (abbreviated IFITM3-M2 AH-imTFP1, Figure 7A). We also constructed a scrambled IFITM3 AH mutant (IFITM3-Scrambled AH-imTFP1) as a control (Figure 7A). When overexpressed in HEK 293/17 cells, wild-type IFITM3 significantly inhibited
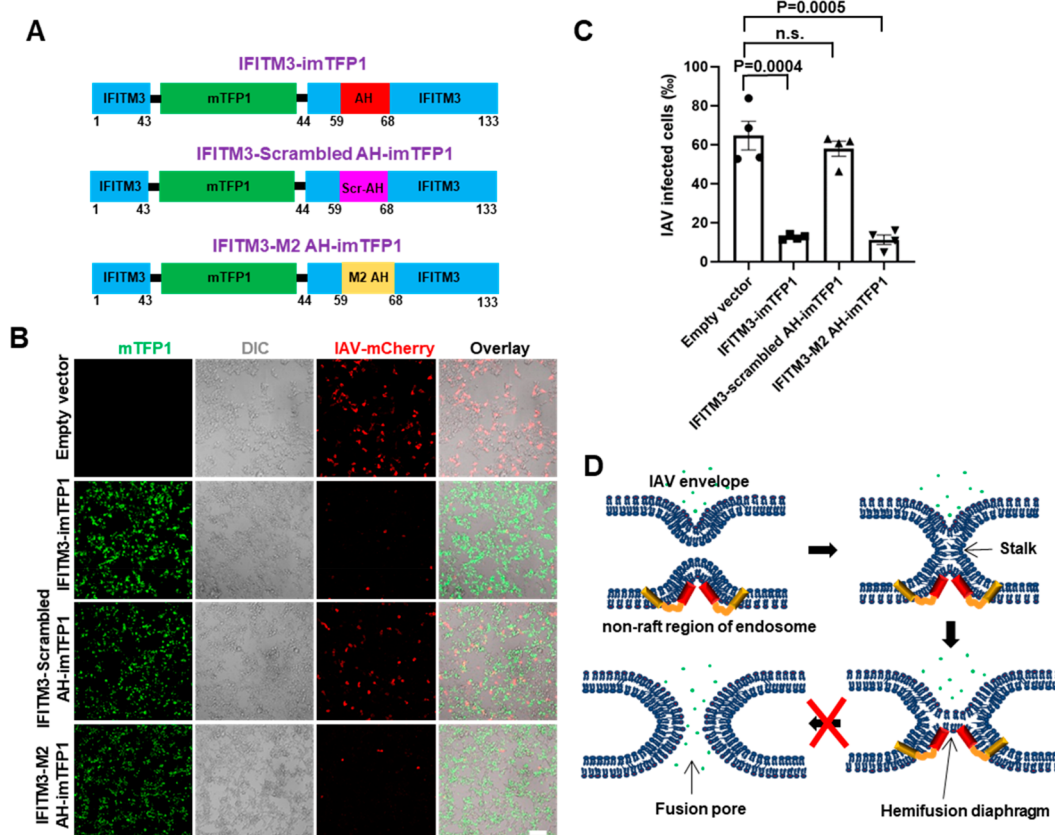
Figure 7. IFITM3 amphipathic helix can be replaced by other negative-curvature-inducing and lipid-ordering amphipathic helices. (A) Illustration of the internal mTFP1-tagged wild-type IFITM3, scrambled IFITM3 AH mutant, and IFITM3 chimera with the influenza virus M2 protein AH. (B) Infection assay of HEK 293T/17 cells expressing wild-type IFITM3-imTFP1, its scrambled mutant, or the M2 AH chimera using mCherry-expressing IAV. Scale bar: 100 μm. (C) Quantification of IAV infection shown in B. Data represent mean ± SEM of the results of four independent experiments. Total number of cells counted are empty vector (3813), IFITM3-imTFP1 (3877), IFITM3-scrambled AH-imTFP1 (3525), and IFITM3-M2 AH-imTFP1 (4244). (D) Working model of IFITM3-mediated inhibition of IAV entry. IFITM3 localizes to liquid disordered subdomains of the endosomal membrane, which are the sites supporting IAV fusion, and stabilizes the hemifusion diaphragm by inducing negative membrane curvature and increasing lipid ordering and membrane stiffness. This prevents the formation of a fusion pore in the hemifusion intermediate, thus trapping IAV at a "dead-end" hemifusion stage. See also Figure S8.

the infection of the mCherry-expressing IAV (Figure 7B,C). As expected, the scrambled IFITM3 AH mutant exhibited a markedly attenuated activity against IAV. Importantly, the IFITM3 chimera with the M2 AH showed strong antiviral activity, without significantly affecting cell viability (Figure S8E). The demonstration that IFITM3 AH can be replaced by other negative-curvature-inducing and lipid-ordering AHs further confirms that IFITM3 inhibits viral fusion by modulating the proprieties of the endosomal membrane through its amphipathic helix.

The broad spectrum of enveloped viruses that are restricted by IFITM proteins suggests a universal mechanism for their antiviral activity. This mechanism may involve modifying the properties of the host cell membranes to disfavor fusion pore formation and thereby trapping viral fusion at a "dead-end" hemifusion stage.[21,25] Here, we provided direct evidence for this mechanism by showing that lipid bilayer-reconstituted recombinant IFITM3 induces negative curvature and increases the lipid order and membrane stiffness, thereby disfavoring viral fusion. Importantly, we found that these effects on lipid bilayers *in vitro* are linked to the IFITM3's ability to inhibit viral fusion with cells. Specifically, incorporation of IFITM3 AH into the cytoplasmic leaflet of the plasma membrane inhibits the forced IAV fusion with the plasma membrane

(Figures 6F,G and S8D), whereas its incorporation into the external leaflet of the plasma membrane inhibits exocytosis (Figure 6B). Although exocytic fusion is the topological opposite of viral fusion, it provides a convenient model system for assessing the effects of exogenously added amphipathic peptides and lipids.[56,57] The relatively modest effect of AH on insulin secretion may be due to an insufficiently high concentration of AH at the insulin granule fusion sites on the plasma membrane.

According to the stalk–pore hypothesis,[61,62] membrane fusion proceeds through a series of highly curved intermediates—stalk, hemifusion, and fusion pore—that are characterized by different net curvatures and thus respond differently to changes in lipid shape/composition. The formation of a lipid stalk involves a local disruption and bending of contacting membrane leaflets into a net negative curvature structure (Figure 7D). The hemifusion intermediate is also a net negative curvature structure, whereas the fusion pore possesses a net positive curvature (Figure 7D).[2] Thus, the presence of lipids that induce positive curvature, such as LPC, in the contacting leaflets disfavors the stalk formation, whereas their incorporation into the distal leaflet of a target membrane promotes rupture of the hemifusion diaphragm and fusion pore formation.[57,61,63,64] In contrast, fusion pore formation is

impaired by lipids inducing negative curvature, such as oleic acid (OA).[65] Thus, spontaneous curvature of lipids is an essential determinant of membrane hemifusion and fusion mediated by cellular and viral proteins.[2]

Our experiments demonstrate that IFITM3 AH induces negative curvature of GUVs, which is manifested in inward budding and ILV formation. Thus, in the context of IFITM3 expressed in cells, AH inserted into the cytoplasmic leaflet of an endosomal membrane is expected to stabilize the hemifusion diaphragm formed by incoming viruses and thus prevent the fusion pore formation (Figure 7D). In addition, the increased membrane order and stiffness induced by IFITM3 are expected to further disfavor membrane fusion.[16−19] These different effects on the membrane's mechanical properties caused by IFITM3 AH may have a compound inhibitory outcome on membrane fusion, since any effects that counteract membrane restructuring are expected to directly influence the kinetics and the efficiency of fusion.[66,67]

Our finding that IFITM3 induces negative curvature and inward budding in GUVs is consistent with the observation that its overexpression in cells robustly induces the formation of large multivesicular bodies that are full of IFITM3-containing intralumenal vesicles.[8] These results also support the "fusion decoy" model, according to which excess of intralumenal vesicles in IFITM3-expressing cells favors non-productive viral fusion with intralumenal vesicles, instead of fusion with the limiting membrane of endosomes.[21] The above considerations suggest that a potent inhibition of diverse enveloped viruses by IFITM3 may involve a combination of modulation of membrane properties and generation of an excess of decoy vesicles in endosomes.

Since most AHs known to date induce positive curvatures,[35] assessment of the mechanism by which the IFITM3 AH induces a negative curvature is obviously an important and interesting subject. However, insights into the molecular mechanism of IFITM3 AH-induced negative curvature would require detailed structural analyses of IFITM3 or its AH peptide in membranes and of their effects on the lipid structure and dynamics. In this study, we show that IFITM3 AH increases lipid order. It is thus reasonable to speculate that the increased lipid order (decrease of area per lipid) in the AH-interacting monolayer might induce negative curvature.[68] It is possible, for example, that the observed negative curvature generation occurs through lipid condensation induced by the adsorption of the peptide on the outer membrane leaflet, an effect analogous to that of calcium ions, which upon adsorption onto negatively charged membranes induce negative curvature.[69,70] Alternatively, unlike the positive-curvature-inducing peptides, AH may promote negative curvature by penetrating deeper into the hydrophobic milieu of lipid bilayers and splaying the acyl chains apart.[71]

Lipid raft domains have been proposed to be the entry sites of viruses due to the raft localization of certain signaling proteins and receptors.[44] However, direct evidence supporting this model is lacking due, in part, to the dynamic nature of raft micro- and nanodomains in living cells.[72] In addition, the rigid nature of lipid raft domains is expected to disfavor membrane fusion. Interestingly, it has been reported that the boundaries between ordered and disordered lipid domains, which are characterized by high line tension (energy per unit length), are the predominant sites of HIV-1 fusion.[73] However, such apparent preference for domain boundaries is not universal, since IAV lipid mixing occurs efficiently with Ld-phased GUVs

lacking lipid rafts or phase boundaries (Figure 4F). No lipid mixing could be detected with Lo GUVs. IFITM3 AH and full-length IFITM3 clearly prefer the Ld phase in phase-separated GUVs/GPMVs, which are powerful models for studying the microdomain localization of membrane proteins. However, imaging of IFITM3 localization in microdomains of endosomes, which is more physiologically relevant to its function, is technically very challenging. We will attempt to address this question in the future by super-resolution microscopy. A correlation between the apparent IAV fusion site and the IFITM3 localization to the Ld phase may offer a clue regarding the potential mechanism of virus resistance. It is tempting to speculate that IFITM3-resistant viruses, like Lassa virus, may localize to and fuse with lipid raft domains devoid of this restriction factor.

It is worth pointing out that AH is present in IFITM1 and IFITM2 proteins and is highly conserved across vertebrates.[17,34] It is therefore very likely that the AH region is key to the antiviral activity of all three human restriction factors. Clearly, this proximity-based antiviral mechanism is dependent on proper trafficking of IFITMs to ensure their concentration at the sites of virus entry.[19,25] Accordingly, incorporation of IFTIMs into virions ensures their presence at the site of fusion and effectively inhibits infection of nearly all tested viruses, including those that are otherwise resistant to IFITM restriction when expressed in target cells.[25,26,74]

CONCLUSIONS

Our findings reveal a universal defense mechanism employed by cells to effectively ward off invading enveloped viruses through modification of the cytoplasmic leaflet of cellular membranes. The IFITM AH-mediated increases in negative curvature and stiffness of the cytoplasmic leaflet disfavor the transition from hemifusion to full fusion and thereby block entry of diverse enveloped viruses. This restriction mechanism informs us of antiviral strategies targeting the cytoplasmic leaflet of cell membranes.

METHODS/EXPERIMENTAL

Key Resources, Cell Lines, and Peptides. Key resources used in this study, including antibodies, recombinant proteins, chemicals, bacterial and virus strains, cell lines, and software are shown in Table S1.

HEK293*T*/17 and A549 cells were maintained in Dulbecco's modified Eagle medium (DMEM, Corning, Corning, NY, USA) containing 10% heat-inactivated fetal bovine serum (FBS, Atlanta Biologicals, Flowery Branch, GA, USA) and 1% penicillin/streptomycin (Gemini Bioproducts, West Sacramento, CA, USA). For HEK 293T/17 cells, the growth medium was supplemented with 0.5 mg/mL G418 (Genesee Scientific, San Diego, CA, USA). INS-1E cells were maintained in RPMI-1640 medium (Addexbio), supplemented with 10% heat-inactivated FBS, 10 mM HEPES, and 55 μM β-mercaptoethanol (Invitrogen, Carlsbad, CA, USA). mCherry-expressing IAV PR/8/34 was a gift from Dr. Luis Martinez-Sobrido (University of Rochester).

N-Terminally Cy5-labeled peptides were synthesized and purified to >95% purity by Gen-Script (Piscataway, NJ, USA). Peptide sequences used were AH(56−71), Cy5-DHVVWSLFNTLFMNPC; scrambled AH(56−71), Cy5-LVWHMFLSDNFTNPV; AH(59−68), Cy5-CVWSLFNTLFM; and AH(59−68) F63Q, Cy5-CVWSLQNTLFM. The fluorescently labeled, palmitoylated IFTIM3 peptide (FITC-Ahx-DHVVWSLFNTLFMNPC(PAL)-CLGF) was chemically synthesized on Rink Amide MBHA resin using Fmoc solid phase peptide synthesis and Fmco-Cys(Mmt)-OH and Fmoc-Ahx-OH, among other Fmoc-protected amino acids. After

chain assembly, the Fmoc group of the N-terminus was removed and extended by the linker amino acid Ahx, followed by the coupling of fluorescein isothiocyanate (FITC, 2 equiv) and DIPEA (2 equiv) in DMF (6 mL) at room temperature overnight. The monomethoxytrityl (Mmt) group was removed with diluted TFA (2%, DCM) and scavengers (10% TIPS), followed by the addition of palmitic anhydride (10 equiv) dissolved in DCM and DIEA (20 equiv) for 3 h. After cleavage from the resin and precipitation with cold diethyl ether, the crude peptide was purified by revered phase HPLC, and its molecular mass verified by ESI-MS.

Protein Expression and Purification. The IFITM3 gene was PCR-amplified and cloned into the pET28a vector to produce recombinant proteins fused to Strep-tag II (WSHPQFEK). Point mutations and deletions were introduced by site-directed mutagenesis. The IFITM3 constructs were transformed into *Escherichia coli* Rosetta 2 (DE3) pLysS singles competent cells to overexpress the proteins. The bacteria were cultured in Terrific broth medium at 37 °C. Protein expression was induced by the addition of 0.3 mM IPTG when OD_{600} was 1.0, and the sample was cultured for an additional 20 h at 16 °C. Cells were harvested after centrifugation at 2500g for 30 min, resuspended, and sonicated in HND buffer (25 mM HEPES, pH 7.4, 150 mM NaCl, 1 mM DTT) supplemented with cOmplete EDTA-free protease inhibitor cocktail (Roche, Basel, Switzerland). The lysate was then centrifuged at 4 °C in the SW32Ti rotor with a speed of 30 000 rpm for 1 h to pellet the membrane fraction using an Optima L-90K ultracentrifuge (Beckman Instruments, Brea, CA, USA). The pellet was resuspended in HND buffer, and bulk membrane proteins were extracted by adding 2% ANAPOE-X-100 and incubating for 1 h at 4 °C, followed by a 1 h centrifugation at 30 000 rpm. The supernatant was loaded on Strep-Tactin resin (QUIGEN, Hilden, Germany), incubated for 3 h at 4 °C, and the column was washed twice with 15 mL of HND buffer supplemented with 0.1% ANAPOE-X-100. Proteins were eluted by adding 10 mL of HND buffer supplemented with 0.1% ANAPOE-X-100 and 2.5 mM desthiobiotin and then concentrated using an Amicon Ultra 5000 MW cutoff filter (Millipore, Billerica, MA, USA). Protein purity was assessed by SDS-PAGE and Coomassie Blue staining. For purification of wild-type and mutant transmembrane-truncated IFITM3, the cell lysate was cleared by centrifugation at 4 °C with at 18 000 rpm for 45 min after sonication, and the supernatant was directly loaded on Strep-Tactin resin, incubated for 3 h at 4 °C, and washed and eluted with the buffer used for purification of the full-length IFITM3 except that ANAPOE-X-100 was omitted.

Large Unilamellar Vesicles. Lipids (99.0 mol % POPC, 0.5 mol % cholesterol, 0.5 mol % Liss-Rho-PE) were mixed in a glass tube and dried down to a film under a gentle stream of argon, followed by further drying under a vacuum for 30 min. Next, the lipid film was hydrated and resuspended with HND buffer to a final lipid concentration of 10 mM. LUVs were formed from the lipid suspension by 10 freeze−thaw cycles using liquid nitrogen and a room-temperature water bath. Uniform-sized LUVs were formed by extruding through polycarbonate filters with 100 nm pore size (Avanti Polar Lipids, Alabaster, AL, USA) 11 times.

To reconstitute IFITM3, preformed liposomes and purified IFITM3 (molar protein to lipid ratio, 1:500) were mixed with 0.1% Triton X-100 at an effective detergent to lipid ratio of ∼1 and incubated for 1 h at 4 °C. Triton X-100 was then removed by adding BioBeads SM-2 absorbent beads at a Bio-Beads/Triton X-100 ratio of 10 (w/w) in five portions during the course of an hour and incubating overnight after the final addition of beads. Insoluble protein aggregates were pelleted by centrifugation of samples in an Eppendorf microcentrifuge (10 min, 16000g).

Liposome Co-floatation Assay. Peptide binding to LUVs was measured by mixing 204 μL of proteoliposomes with 600 μL of a 67% sucrose solution, bringing the final sucrose concentration to 50%. The mixture was transferred to a clear polycarbonate ultracentrifuge tube and overlaid with two layers consisting of 10.2 mL of 25% sucrose and 1 mL of 5% sucrose. After centrifugation at 30 000 rpm (4 °C for 3 h) in the SW45Ti rotor (Beckman Instruments), eight 1.5 mL fractions

were collected from the top of a gradient. Aliquots of 30 μL from each fraction were analyzed by Western blotting with IFITM3 antibody.

Trypsin Cleavage Assay. To determine the accessibility of LUV-reconstituted peptides, 20 μL of proteoliposomes was incubated with 0.6 μg of trypsin (TPCK-Treated, Sigma-Aldrich) at 37 °C for 30 min. Next, 95 °C preheated SDS sample buffer (50 mM Tris-HCl, pH 6.8, 2% SDS, 10% glycerol, 1% β-mercaptoethanol, 12.5 mM EDTA, 0.02% bromophenol blue) was added to stop the reaction. The samples were analyzed by SDS-PAGE and stained with Coomassie blue.

Liposome Co-sedimentation Assay. Peptides were sonicated in a water bath for 30 min, and possible aggregates were removed by spinning down at 20000g for 5 min. LUVs (2 mM) made of 99.0 mol % POPC, 0.5 mol % cholesterol, and 0.5 mol % Liss-Rho-PE in PBS were incubated at room temperature with 20 μM IFITM3(1-108)-iEGFP protein or 40 μM Cy5-labeled peptides for 10 min in a 100 μL reaction volume. The mixture was then diluted with PBS and centrifuged at 30 000 rpm for 30 min at 20 °C. Fluorescence of the supernatant was measured on a SpectraMax i3x microplate reader (Molecular Devices, CA, USA). The binding efficiency of proteins/peptides was decided by reduction of EGFP or Cy5 fluorescence in the supernatant and normalized by comparing with the fluorescence of input samples.

Giant Unilamellar Vesicles. GUVs were prepared from a 5 mM solution of lipids in chloroform (99 mol % POPC, 0.5 mol % cholesterol, and 0.5 mol % of Liss-Rho-PE). A 50 μL amount of the lipid solution was spread onto a 10 cm^2 area of the conductive side of each of two indium−tin oxide (ITO)-coated slides (70−100 Ω, Delta Technologies, Stillwater, MN, USA), allowed to evaporate, and kept under vacuum for 1 h. Electroformation chambers were constructed by sandwiching a 1 mm spacer between two lipid-coated slides. Next, the chamber was filled with 0.1 M sucrose and 1 mM HEPES, pH 7.0, and a 10 Hz sine wave voltage (1 V peak-to-peak) was applied across the chamber for 3 h using a function generator. GUVs were gently collected with a pipet and used immediately.

To prepare phase-separated GUVs, we used a mixture of 33 mol % DOPC, 33 mol % SM, 33 mol % cholesterol, 0.5% TopFluor-cholesterol, and 0.5% Liss-Rho-PE. Lipids were dissolved in 50 μL of chloroform/methanol (9:1) in a glass tube and placed in a preheated block at 60 °C for 1 min after gentle vortexing and centrifugation. The mixture was then immediately deposited and spread over two preheated ITO coverslips, and the solvent was evaporated at 60 °C. After the ITO coverslips dried out, they were immediately placed into a vacuum chamber for 1 h to remove residual solvent. All these steps were done in a timely manner to minimize possible lipid oxidation. GUV electroformation was carried out in 0.1 M sucrose, 2 mM DTT, and 1 mM HEPES, pH 7.0, at 60 °C for 4 h. Collected GUVs were cooled to room temperature and used immediately.

For imaging of GUVs with IFITM3 peptides, peptides were prepared as 2 mg/mL stock solutions in DMSO. A 20 μL amount of GUVs was diluted in 30 μL of a hypertonic buffer containing160 mM sucrose and 1 mM HEPES, pH 7.0, to slightly deflate GUVs. Next, 2 μL of peptide diluted with 98 μL of Hank's balanced salt solution (Corning, NY, USA) was added to and mixed with GUVs, yielding the final concentration of peptide of 10 μM. The mixture of GUVs and peptide was immediately added to an eight-well chambered coverslip pretreated with a BSA solution (2 mg/mL) for 30 min to attach GUVs to the bottom of the chamber. GUVs were allowed to sediment for 10 min before imaging on a Zeiss LSM880 laser scanning confocal microscope, using a 63×/1.4 NA oil-immersion objective. Purified wild-type and mutant transmembrane-truncated IFITM3 proteins were imaged the same way except that the final concentration of proteins was 20 μM. Quantification of inward budding of GUVs was performed by counting all GUVs with a diameter above 2 μm, regardless of whether they encompassed intraluminal vesicles containing aqueous dye (fluorescein or EGFP). Images of at least two randomly selected fields of view were acquired using Z-stacks separated by 1 μm. For each condition, at least two independent experiments were performed.

GUVs containing IFITM3 protein were prepared through dehydration of IFITM3-containing LUVs, as previously described.[28] Briefly, IFITM3-containing LUVs were prepared, as above, added dropwise onto ITO-coated slides, and dehydrated under vacuum overnight. The lipids were rehydrated and electroformed in 0.1 M sucrose/1 mM HEPES, pH 7.0, as described above at room temperature for 6 h, and GUVs were gently collected with a pipet and imaged immediately.

A tube-pulling assay of GUV was performed using a methodology similar to that previously described.[36] Briefly, GUVs containing 98 mol % POPC, 0.5 mol % 18:1 biotinyl Cap PE, 0.5 mol % cholesterol, and 0.5 mol % of Liss-Rho-PE were formed. GUVs were immobilized on a 0.1% BSA−biotin-coated glass by incubating with 0.2 mg/mL streptavidin. Tubes were pulled applying a shear force to tethered GUVs. Cy5-AH(59−68) peptide (10 μM) was added after tube formation and imaged immediately.

Plasma Membrane Spheres. Plasma membrane spheres (PMSs) were prepared as previously described.[50] Briefly, A549 cells stably expressing IFITM3-iSNAP were seeded on an eight-well chambered coverslip. Twenty-four hours later cells were washed and incubated for 18 h in PMS buffer (1.5 mM $CaCl_2$, 1.5 mM $MgCl_2$, 5 mM HEPES, pH 7.4, 1 mg/mL glucose in 1× PBS) at 37 °C. The lipid ordered phase was visualized through GM1 cross-linking by incubating the PMSs in 10 μg/mL of Alexa-488-labeled cholera-toxin subunit B (Invitrogen) for 2 h at 37 °C, and IFITM3-iSNAP was stained with 3 μM SNAP-cell 647-SIR (New England Biolabs) at the same time. PMSs were then washed and imaged at room temperature on a Zeiss LSM880 laser scanning confocal microscope, using a 63×/1.4 NA oil-immersion objective.

Lipid Mixing between Influenza Virus and GUVs. Virus labeling was performed essentially as described previously.[25] Briefly, a 100 μL aliquot of the 2 mg/mL influenza A/PR/8/34 virus stock (Charles River, CT, USA) was thawed at room temperature and diluted using 50 μL of isotonic 145 mM NaCl/50 mM HEPES (pH 7.4) buffer. To label the virus membrane, 1.5 μL of DiD dye (10 mM stock solution in DMSO) was quickly injected into a mixture during mild vortexing to a final concentration of 100 μM. The tube was closed, wrapped with aluminum foil, and agitated at the lowest speed setting of the vortex for 1 h at room temperature. The labeled viruses were purified from excess dyes on a Nap-5 gel filtration column (GE Healthcare) that was equilibrated with 50 mM HEPES, pH 7.4, and 145 mM NaCl at room temperature. The fractions containing labeled viruses were passed through a 0.45 μm filter to remove any large lipid and/or virus aggregates. To test the labeling efficiency, 10 μL of the purified viruses was diluted to 1000 μL in PBS and lysed with 0.5% TX-100 (final concentration), and the extent of DiD dequenching was measured in a plate reader. A more than 20-fold increase in the DiD signal upon lysis has been found to give good results in lipid mixing experiments. The labeled virus was aliquoted into tubes, flash-frozen, and stored at −80 °C until use. The virus lipid mixing assay was performed by mixing 20 μL of the labeled virus with 30 μL of GUVs, followed by addition of 150 μL of 100 mM citrate buffer (pH 4.8) supplemented with 100 mM MES to achieve the final pH of 5.0. The resulting mixture was transferred into a BSA-pretreated eight-well coverslip and imaged on a Zeiss LSM880 laser scanning confocal microscope, using a 63×/1.4 NA oil-immersion objective.

Lipid Order Measurement. To assess the lipid order, 2 mM LUVs were mixed with 25 μM Laurdan dye (Invitrogen) and 40 μM of the indicated IFITM3-derived peptide in a total volume of 50 μL. Fluorescence was measured on a SpectraMax i3x microplate reader using a 355 nm excitation filter and recording fluorescence emissions at two wavelengths centered at 440 and 490 nm. Laurdan general polarization was calculated using the equation $GP = (I_{440} - I_{490})/(I_{440} + I_{490})$, where I_{440} and I_{490} are fluorescence intensities at 440 and 490 nm, respectively.

Membrane Bending Rigidity Measurement. GUVs were grown on a poly(vinyl alcohol) (PVA) film as described previously.[75] Briefly, 50 μL of a 5% w/v (145 000 g/mol) PVA (Merck) solution in water was spread on a cleaned (rinsed in ethanol and double-distilled water) glass slide to form a thin film. The PVA film was dried kept in

the oven at 50 °C for 30 min. Five μL of a 2 mM lipid solution (80 mol % POPC, 20 mol % cholesterol) in chloroform was spread on the PVA film, and the solvent was evaporated under vacuum for 1 h. An observation chamber with a volume of about 700 μL was assembled using a Teflon spacer sandwiched between two glasses with the lipid film facing inward, and the lipid films were hydrated in a solution of 100 mM sucrose (Sigma) and 1 mM HEPES (Sigma) at pH 7.4. After swelling for 30 min, GUVs were harvested and used right away. An aliquot of 0.1 μL of DMSO solution with or without the peptide was carefully pipetted into 100 μL of GUV suspension and slowly agitated to ensure mixing. Subsequently, 30 μL of the final solution was placed on a BSA-coated glass coverslip. A few percent of the solution was left to evaporate for 3 to 5 min in ambient air and then closed in an observation chamber. Bending rigidity analysis was performed either on vesicles with added DMSO only (control) or DMSO with IFITM3 at a final concentration of the peptide of 3 nM. Membrane bending rigidity was measured by fluctuation analysis of the thermally induced motion of the membrane, as described previously.[54] Experiments were performed on an Axio Observer D1 microscope (Zeiss, Germany) using a 40× objective in phase contrast mode. Imaging was performed using a low-noise liquid-cooled digital camera, pco.edge 5.5, and a total of 1000−2000 snapshots per vesicle were acquired with exposure time of 200 μs at 10 frames per second. The bending rigidity κ is estimated from $\kappa/k_BT = S(q)/\langle|v_q|^2\rangle$, where $S(q)$ is a perfector that depends on the membrane tension, k_BT is the thermal energy, and $|v_q|^2$ is calculated from the experimentally obtained spectrum.

Insulin Secretion Assay. An insulin secretion assay was performed, as described previously[56] with some modifications. Briefly, a lentivirus vector expressing luciferase fusion protein was produced using a second-generation viral packaging system. A 4 μg amount of pLX304 vector containing the fusion construct Proinsulin-NanoLuc, 2 μg of psPAX2 packaging plasmid, and 2 μg of pMD2.G envelope plasmid were used to transfect a 10 cm dish of HEK 293T/17cells using JetPRIME transfection reagent. Virus was harvested at 48 h post-transfection and passed through 0.45 μm cellulose acetate filters prior to use. Viruses were spun onto INS-1E cells at 800g for 1 h at 30 °C. After 24 h at 37 °C in 5% CO_2 in the presence of virus, the medium was placed in fresh growth media with 5 μg/mL blasticidin (Invitrogen) for 3 days to select for infected cells. For insulin secretion assays, INS-1E cells were plated in 96-well plates and cultured overnight at 37 °C in 5% CO_2. Cells were washed once with PBS and incubated for 1 h at 37 °C in sterile, 0.45-μm-filtered Krebs ringer buffer (KRB) containing 138 mM NaCl, 5.4 mM KCl, 2.6 mM $MgCl_2$, 2.6 mM $CaCl_2$, 5 mM $NaHCO_3$, 10 mM HEPES, and 5 g/L BSA (Sigma), supplemented with 2.8 mM glucose. The cells were then incubated with 2 μM of the indicated IFITM3 peptides in KRB for 5 min and then stimulated for 20 min in 100 μL of fresh KRB with 20 mM glucose. For the time course study, after incubating the cells for 1 h in 2.8 mM glucose KRB, the buffer was changed every 5 min to fresh, prewarmed to 37 °C KRB containing either 2.8 mM glucose (for the first time point) or 20 mM glucose (for all subsequent time points). The luciferase signal in samples was determined by adding the coelenterazine substrate (NanoLight, Pinetop, AZ, USA) to the supernatant to a final concentration of 10 μM and reading on a TopCount NXT luminescence counter.

Virus Production, Infection, and Fusion Assays. IAV pseudoviruses were produced by transfecting HEK293T/17 cells using JetPRIME transfection reagent (Polyplus-transfection, SA, NY, USA), as described previously.[76] For producing luciferase-expressing IAV pseudoviruses, HEK293T/17 cells grown in a 100 mm dish were transfected with 2.5 μg of pCAGGS plasmid expressing H1N1 HA and NA proteins, 4 μg of NL4-3R$^-$E$^-$Luc, and 1 μg of pcRev. To generate BlaM-Vpr IAV pseudoviruses, the cells were transfected as above, except 4 μg of pR9ΔEnv (instead of NL4-3R$^-$E$^-$Luc) and 2 μg of BlaM-Vpr were added to the mix. The transfection medium was replaced with fresh DMEM/10% FBS after 12 h, and cells were cultured for an additional 36 h, after which time the virus-containing culture medium was collected, passed through a 0.45 μm filter, and concentrated 10× using Lenti-X concentrator (Clontech, Mountain View, CA, USA). Following an overnight concentration with Lenti-X,

virus was precipitated by centrifuging at 1439g for 45 min at 4 °C, resuspended in DMEM without phenol red or FBS, and stored at −80 °C. Infection assays were performed using HEK 293T/17 cells transfected with the indicated IFITM3 constructs in pcDNA3.1(+) vector using JetPRIME transfection reagent. At 24 h post-transfection, pseudoviruses (0.1 ng of p24) were spinoculated onto cells at 1500g, 4 °C for 30 min, and cells were cultured for 24 h. Luciferase activity was determined by adding Bright-Glo Luciferase substrate (Promega, WI, USA, USA) and reading with a TopCount NXT luminescence counter (PerkinElmer, Waltham, MA, USA).

For infection of mCherry-expressing IAV PR8 virus, HEK 293T/17 cells were seeded on an eight-well chambered coverslip 24 h before transfection with indicated IFITM3 constructs in pQCXIP. At 12 h post-transfection, mCherry-expressing IAV PR8 virus (2.5×10^4 PFU/mL) was spinoculated onto cells at 1500g, 4 °C, for 30 min, and cells were cultured for 12 h and imaged on a Zeiss LSM880 laser scanning confocal microscope, using a 20× objective.

For forced fusion of mCherry-expressing IAV PR8 virus with the plasma membrane, stable A549 cell lines expressing EGFP-CAAX, EGFP-IFITM3 AH-CAAX, or EGFP-IFITM3 AH CAAX were produced using the second-generation viral packaging system, as described above. Cells were seeded on eight-well chambered coverslips and cultured for 24 h at 37 °C in 5% CO_2. The cells were then incubated with 100 nM Bafilomycin A1 for 30 min at 37 °C in 5% CO_2, and mCherry-expressing IAV PR8 virus (1×10^5 PFU/mL) was spinoculated onto cells at 1500g, 4 °C, for 30 min. Cells were washed once with cold PBS to remove unbound viruses and were incubated with warm 100 mM citrate buffer, pH 4.0, at 37 °C in 5% CO_2 for 15 min. Next, the cells were washed with warm PBS and cultured in medium containing 100 nM Bafilomycin A1 at 37 °C in 5% CO_2 for 12 h and imaged on a Zeiss LSM880 laser scanning confocal microscope, using a 20× objective.

For forced fusion of β-lactamase-Vpr IAV (IAV/BlaM-Vpr) pseudotyped viruses at the plasma membrane, confluent A549-expressing EGFP-CAAX, EGFP-IFITM3 AH-CAAX, or EGFP-IFITM3 AH CAAX seeded in a 96-well black clear bottom plate (Corning) were pretreated with 50 nm Bafilomycin A1 for 30 min at 37 °C, 5% CO_2. IAV/BlaM-Vpr pseudoviruses (0.5 ng of p24/well) were bound to the cells, as described above. The unbound virus was removed, and the cells were exposed to either a prewarmed pH 5.0 MES-citrate buffer or a neutral buffer for 10 min at 37 °C, 5% CO_2. After replacing the respective buffers, cells were cultured in a growth medium containing 50 nM Bafilomycin A1 at 37 °C, 5% CO_2, for 2 h, after which the samples were placed on ice, loaded with FRET CCF4-AM substrate (Invitrogen), and incubated overnight at 11 °C, and the BlaM activity (blue to green ratio) was measured using a SpectraMaxi3 plate reader.

Statistical Analysis. All data were analyzed using GraphPad Prism software by unpaired t test.

ASSOCIATED CONTENT

Ⓢ Supporting Information

The Supporting Information is available free of charge at https://pubs.acs.org/doi/10.1021/acsnano.0c10567.

> Supplemental appendix; additional figures; and a table of key resources used in this study (PDF)

> Supplemental Video 1: 3D image series of GUVs containing ILVs and nanotubes (AVI)

AUTHOR INFORMATION

Corresponding Author

Gregory B. Melikyan − *Department of Pediatrics, Emory University School of Medicine, Atlanta, Georgia 30322, United States; Children's Healthcare of Atlanta, Atlanta, Georgia 30322, United States;* ⓞ orcid.org/0000-0001-5385-3013; Email: gmeliki@emory.edu

Authors

Xiangyang Guo − *Department of Pediatrics, Emory University School of Medicine, Atlanta, Georgia 30322, United States;* ⓞ orcid.org/0000-0002-8463-2755

Jan Steinkühler − *Max Planck Institute of Colloids and Interfaces, 14424 Potsdam, Germany;* ⓞ orcid.org/0000-0003-4226-7945

Mariana Marin − *Department of Pediatrics, Emory University School of Medicine, Atlanta, Georgia 30322, United States*

Xiang Li − *School of Pharmacy, Second Military Medical University, Shanghai 200433, China*

Wuyuan Lu − *Institute of Human Virology and Department of Biochemistry and Molecular Biology, University of Maryland School of Medicine, Baltimore, Maryland 21201, United States;* ⓞ orcid.org/0000-0003-1318-9968

Rumiana Dimova − *Max Planck Institute of Colloids and Interfaces, 14424 Potsdam, Germany*

Complete contact information is available at:
https://pubs.acs.org/10.1021/acsnano.0c10567

REFERENCES

(1) Harrison, S. C. Viral Membrane Fusion. *Nat. Struct. Mol. Biol.* **2008**, *15*, 690−698.

(2) Chernomordik, L. V.; Kozlov, M. M. Protein-Lipid Interplay in Fusion and Fission of Biological Membranes. *Annu. Rev. Biochem.* **2003**, *72*, 175−207.

(3) Brass, A. L.; Huang, I. C.; Benita, Y.; John, S. P.; Krishnan, M. N.; Feeley, E. M.; Ryan, B. J.; Weyer, J. L.; van der Weyden, L.; Fikrig, E.; Adams, D. J.; Xavier, R. J.; Farzan, M.; Elledge, S. J. The IFITM Proteins Mediate Cellular Resistance to Influenza A H1N1 Virus, West Nile Virus, and Dengue Virus. *Cell* **2009**, *139*, 1243−1254.

(4) Diamond, M. S.; Farzan, M. The Broad-Spectrum Antiviral Functions of IFIT and IFITM Proteins. *Nat. Rev. Immunol.* **2013**, *13*, 46−57.

(5) Mudhasani, R.; Tran, J. P.; Retterer, C.; Radoshitzky, S. R.; Kota, K. P.; Altamura, L. A.; Smith, J. M.; Packard, B. Z.; Kuhn, J. H.; Costantino, J.; Garrison, A. R.; Schmaljohn, C. S.; Huang, I. C.;

Farzan, M.; Bavari, S. IFITM-2 and IFITM-3 but Not IFITM-1 Restrict Rift Valley Fever Virus. *J. Virol* **2013**, *87*, 8451−8464.

(6) Huang, I. C.; Bailey, C. C.; Weyer, J. L.; Radoshitzky, S. R.; Becker, M. M.; Chiang, J. J.; Brass, A. L.; Ahmed, A. A.; Chi, X.; Dong, L.; Longobardi, L. E.; Boltz, D.; Kuhn, J. H.; Elledge, S. J.; Bavari, S.; Denison, M. R.; Choe, H.; Farzan, M. Distinct Patterns of IFITM-Mediated Restriction of Filoviruses, SARS Coronavirus, and Influenza A Virus. *PLoS Pathog.* **2011**, *7*, No. e1001258.

(7) Feeley, E. M.; Sims, J. S.; John, S. P.; Chin, C. R.; Pertel, T.; Chen, L. M.; Gaiha, G. D.; Ryan, B. J.; Donis, R. O.; Elledge, S. J.; Brass, A. L. IFITM3 Inhibits Influenza A Virus Infection by Preventing Cytosolic Entry. *PLoS Pathog.* **2011**, *7*, No. e1002337.

(8) Amini-Bavil-Olyaee, S.; Choi, Y. J.; Lee, J. H.; Shi, M.; Huang, I. C.; Farzan, M.; Jung, J. U. The Antiviral Effector IFITM3 Disrupts Intracellular Cholesterol Homeostasis to Block Viral Entry. *Cell Host Microbe* **2013**, *13*, 452−464.

(9) Bailey, C. C.; Huang, I. C.; Kam, C.; Farzan, M. IFITM3 Limits the Severity of Acute Influenza in Mice. *PLoS Pathog.* **2012**, *8*, No. e1002909.

(10) Everitt, A. R.; Clare, S.; McDonald, J. U.; Kane, L.; Harcourt, K.; Ahras, M.; Lall, A.; Hale, C.; Rodgers, A.; Young, D. B.; Haque, A.; Billker, O.; Tregoning, J. S.; Dougan, G.; Kellam, P. Defining the Range of Pathogens Susceptible to IFITM3 Restriction Using a Knockout Mouse Model. *PLoS One* **2013**, *8*, No. e80723.

(11) Everitt, A. R.; Clare, S.; Pertel, T.; John, S. P.; Wash, R. S.; Smith, S. E.; Chin, C. R.; Feeley, E. M.; Sims, J. S.; Adams, D. J.; Wise, H. M.; Kane, L.; Goulding, D.; Digard, P.; Anttila, V.; Baillie, J. K.; Walsh, T. S.; Hume, D. A.; Palotie, A.; Xue, Y.; et al. IFITM3 Restricts the Morbidity and Mortality Associated with Influenza. *Nature* **2012**, *484*, 519−523.

(12) Zhang, Y. H.; Zhao, Y.; Li, N.; Peng, Y. C.; Giannoulatou, E.; Jin, R. H.; Yan, H. P.; Wu, H.; Liu, J. H.; Liu, N.; Wang, D. Y.; Shu, Y. L.; Ho, L. P.; Kellam, P.; McMichael, A.; Dong, T. Interferon-Induced Transmembrane Protein-3 Genetic Variant RS12252-C Is Associated with Severe Influenza in Chinese Individuals. *Nat. Commun.* **2013**, *4*, 1418.

(13) Bailey, C. C.; Kondur, H. R.; Huang, I. C.; Farzan, M. Interferon-Induced Transmembrane Protein 3 Is a Type II Transmembrane Protein. *J. Biol. Chem.* **2013**, *288*, 32184−32193.

(14) Ling, S.; Zhang, C.; Wang, W.; Cai, X.; Yu, L.; Wu, F.; Zhang, L.; Tian, C. Combined Approaches of EPR and NMR Illustrate Only One Transmembrane Helix in the Human IFITM3. *Sci. Rep.* **2016**, *6*, 24029.

(15) Weston, S.; Czieso, S.; White, I. J.; Smith, S. E.; Kellam, P.; Marsh, M. A Membrane Topology Model for Human Interferon Inducible Transmembrane Protein 1. *PLoS One* **2014**, *9*, No. e104341.

(16) John, S. P.; Chin, C. R.; Perreira, J. M.; Feeley, E. M.; Aker, A. M.; Savidis, G.; Smith, S. E.; Elia, A. E.; Everitt, A. R.; Vora, M.; Pertel, T.; Elledge, S. J.; Kellam, P.; Brass, A. L. The CD225 Domain of IFITM3 Is Required for Both IFITM Protein Association and Inhibition of Influenza A Virus and Dengue Virus Replication. *J. Virol* **2013**, *87*, 7837−7852.

(17) Chesarino, N. M.; Compton, A. A.; McMichael, T. M.; Kenney, A. D.; Zhang, L.; Soewarna, V.; Davis, M.; Schwartz, O.; Yount, J. S. IFITM3 Requires an Amphipathic Helix for Antiviral Activity. *EMBO Rep.* **2017**, *18*, 1740−1751.

(18) Lin, T. Y.; Chin, C. R.; Everitt, A. R.; Clare, S.; Perreira, J. M.; Savidis, G.; Aker, A. M.; John, S. P.; Sarlah, D.; Carreira, E. M.; Elledge, S. J.; Kellam, P.; Brass, A. L. Amphotericin B Increases Influenza A Virus Infection by Preventing IFITM3-Mediated Restriction. *Cell Rep.* **2013**, *5*, 895−908.

(19) Li, K.; Markosyan, R. M.; Zheng, Y. M.; Golfetto, O.; Bungart, B.; Li, M.; Ding, S.; He, Y.; Liang, C.; Lee, J. C.; Gratton, E.; Cohen, F. S.; Liu, S. L. IFITM Proteins Restrict Viral Membrane Hemifusion. *PLoS Pathog.* **2013**, *9*, No. e1003124.

(20) Rahman, K.; Coomer, C. A.; Majdoul, S.; Ding, S. Y.; Padilla-Parra, S.; Compton, A. A. Homology-Guided Identification of a

(21) Desai, T. M.; Marin, M.; Chin, C. R.; Savidis, G.; Brass, A. L.; Melikyan, G. B. IFITM3 Restricts Influenza A Virus Entry by Blocking the Formation of Fusion Pores Following Virus-Endosome Hemifusion. *PLoS Pathog.* **2014**, *10*, No. e1004048.

(22) Wu, X.; Spence, J. S.; Das, T.; Yuan, X.; Chen, C.; Zhang, Y.; Li, Y.; Sun, Y.; Chandran, K.; Hang, H. C.; Peng, T. Site-Specific Photo-Crosslinking Proteomics Reveal Regulation of IFITM3 Trafficking and Turnover by VCP/P97 ATPASE. *Cell Chem. Biol.* **2020**, *27*.

(23) Wrensch, F.; Winkler, M.; Pohlmann, S. IFITM Proteins Inhibit Entry Driven by the MERS-Coronavirus Spike Protein: Evidence for Cholesterol-Independent Mechanisms. *Viruses* **2014**, *6*, 3683−3698.

(24) Fu, B.; Wang, L.; Li, S.; Dorf, M. E. ZMPSTE24 Defends against Influenza and Other Pathogenic Viruses. *J. Exp. Med.* **2017**, *214*, 919−929.

(25) Suddala, K. C.; Lee, C. C.; Meraner, P.; Marin, M.; Markosyan, R. M.; Desai, T. M.; Cohen, F. S.; Brass, A. L.; Melikyan, G. B. Interferon-Induced Transmembrane Protein 3 Blocks Fusion of Sensitive but Not Resistant Viruses by Partitioning into Virus-Carrying Endosomes. *PLoS Pathog.* **2019**, *15*, No. e1007532.

(26) Tartour, K.; Nguyen, X. N.; Appourchaux, R.; Assil, S.; Barateau, V.; Bloyet, L. M.; Burlaud Gaillard, J.; Confort, M. P.; Escudero-Perez, B.; Gruffat, H.; Hong, S. S.; Moroso, M.; Reynard, O.; Reynard, S.; Decembre, E.; Ftaich, N.; Rossi, A.; Wu, N.; Arnaud, F.; Baize, S.; et al. Interference with the Production of Infectious Viral Particles and Bimodal Inhibition of Replication Are Broadly Conserved Antiviral Properties of IFITMs. *PLoS Pathog.* **2017**, *13*, No. e1006610.

(27) Rigaud, J. L.; Levy, D. Reconstitution of Membrane Proteins into Liposomes. *Methods Enzymol.* **2003**, *372*, 65−86.

(28) Girard, P.; Pecreaux, J.; Lenoir, G.; Falson, P.; Rigaud, J. L.; Bassereau, P. A New Method for the Reconstitution of Membrane Proteins into Giant Unilamellar Vesicles. *Biophys. J.* **2004**, *87*, 2098−2098.

(29) Karimi, M.; Steinkuhler, J.; Roy, D.; Dasgupta, R.; Lipowsky, R.; Dimova, R. Asymmetric Ionic Conditions Generate Large Membrane Curvatures. *Nano Lett.* **2018**, *18*, 7816−7821.

(30) Steinkuhler, J.; Knorr, R. L.; Zhao, Z.; Bhatia, T.; Bartelt, S. M.; Wegner, S.; Dimova, R.; Lipowsky, R. Controlled Division of Cell-Sized Vesicles by Low Densities of Membrane-Bound Proteins. *Nat. Commun.* **2020**, *11*, 905.

(31) McMahon, H. T.; Gallop, J. L. Membrane Curvature and Mechanisms of Dynamic Cell Membrane Remodelling. *Nature* **2005**, *438*, 590−596.

(32) Julkowska, M. M.; Rankenberg, J. M.; Testerink, C. Liposome-Binding Assays to Assess Specificity and Affinity of Phospholipid-Protein Interactions. *Methods Mol. Biol.* **2013**, *1009*, 261−271.

(33) Angelova, M. I.; Dimitrov, D. S. Liposome Electroformation. *Faraday Discuss. Chem. Soc.* **1986**, *81*, 303.

(34) Zhang, Z.; Liu, J.; Li, M.; Yang, H.; Zhang, C. Evolutionary Dynamics of the Interferon-Induced Transmembrane Gene Family in Vertebrates. *PLoS One* **2012**, *7*, No. e49265.

(35) Drin, G.; Antonny, B. Amphipathic Helices and Membrane Curvature. *FEBS Lett.* **2010**, *584*, 1840−1847.

(36) Pucadyil, T. J.; Schmid, S. L. Real-Time Visualization of Dynamin-Catalyzed Membrane Fission and Vesicle Release. *Cell* **2008**, *135*, 1263−1275.

(37) Sorre, B.; Callan-Jones, A.; Manzi, J.; Goud, B.; Prost, J.; Bassereau, P.; Roux, A. Nature of Curvature Coupling of Amphiphysin with Membranes Depends on Its Bound Density. *Proc. Natl. Acad. Sci. U. S. A.* **2012**, *109*, 173−178.

(38) Helfrich, W. Elastic Properties of Lipid Bilayers - Theory and Possible Experiments. *Z. Naturforsch., C: J. Biosci.* **1973**, *28*, 693−703.

(39) Kozlov, M. M. Determination of Lipid Spontaneous Curvature from X-Ray Examinations of Inverted Hexagonal Phases. *Methods Mol. Biol.* **2007**, *400*, 355−366.

(40) Stachowiak, J. C.; Hayden, C. C.; Sasaki, D. Y. Steric Confinement of Proteins on Lipid Membranes Can Drive Curvature and Tubulation. *Proc. Natl. Acad. Sci. U. S. A.* **2010**, *107*, 7781−7786.

(41) Bassereau, P.; Jin, R.; Baumgart, T.; Deserno, M.; Dimova, R.; Frolov, V. A.; Bashkirov, P. V.; Grubmuller, H.; Jahn, R.; Risselada, H. J.; Johannes, L.; Kozlov, M. M.; Lipowsky, R.; Pucadyil, T. J.; Zeno, W. F.; Stachowiak, J. C.; Stamou, D.; Breuer, A.; Lauritsen, L.; Simon, C.; et al. The 2018 Biomembrane Curvature and Remodeling Roadmap. *J. Phys. D Appl. Phys.* **2018**, 51.

(42) Fuller, N.; Rand, R. P. The Influence of Lysolipids on the Spontaneous Curvature and Bending Elasticity of Phospholipid Membranes. *Biophys. J.* **2001**, *81*, 243−254.

(43) Rajendran, L.; Simons, K. Lipid Rafts and Membrane Dynamics. *J. Cell Sci.* **2005**, *118*, 1099−1102.

(44) Chazal, N.; Gerlier, D. Virus Entry, Assembly, Budding, and Membrane Rafts. *Microbiol. Mol. Biol. Rev.* **2003**, *67*, 226.

(45) Levental, I.; Lingwood, D.; Grzybek, M.; Coskun, U.; Simons, K. Palmitoylation Regulates Raft Affinity for the Majority of Integral Raft Proteins. *Proc. Natl. Acad. Sci. U. S. A.* **2010**, *107*, 22050−22054.

(46) Yount, J. S.; Moltedo, B.; Yang, Y. Y.; Charron, G.; Moran, T. M.; Lopez, C. B.; Hang, H. C. Palmitoylome Profiling Reveals S-Palmitoylation-Dependent Antiviral Activity of IFITM3. *Nat. Chem. Biol.* **2010**, *6*, 610−614.

(47) Kaiser, H. J.; Lingwood, D.; Levental, I.; Sampaio, J. L.; Kalvodova, L.; Rajendran, L.; Simons, K. Order of Lipid Phases in Model and Plasma Membranes. *Proc. Natl. Acad. Sci. U. S. A.* **2009**, *106*, 16645−16650.

(48) Wesolowska, O.; Michalak, K.; Maniewska, J.; Hendrich, A. B. Giant Unilamellar Vesicles - A Perfect Tool to Visualize Phase Separation and Lipid Rafts in Model Systems. *Acta Biochim Pol* **2009**, *56*, 33−39.

(49) Jia, R.; Xu, F. W.; Qian, J.; Yao, Y. F.; Miao, C. H.; Zheng, Y. M.; Liu, S. L.; Guo, F.; Geng, Y. Q.; Qiao, W. T.; Liang, C. Identification of an Endocytic Signal Essential for the Antiviral Action of IFITM3. *Cell. Microbiol.* **2014**, *16*, 1080−1093.

(50) Lingwood, D.; Ries, J.; Schwille, P.; Simons, K. Plasma Membranes Are Poised for Activation of Raft Phase Coalescence at Physiological Temperature. *Proc. Natl. Acad. Sci. U. S. A.* **2008**, *105*, 10005−10010.

(51) Vanblitterswijk, W. J.; Vanhoeven, R. P.; Vandermeer, B. W. Lipid Structural Order Parameters (Reciprocal of Fluidity) in Biomembranes Derived from Steady-State Fluorescence Polarization Measurements. *Biochim. Biophys. Acta, Biomembr.* **1981**, *644*, 323−332.

(52) Parasassi, T.; De Stasio, G.; Dubaldo, A.; Gratton, E. Phase Fluctuation in Phospholipid-Membranes Revealed by Laurdan Fluorescence. *Biophys. J.* **1990**, *57*, 1179−1186.

(53) Steinkuhler, J.; Sezgin, E.; Urbancic, I.; Eggeling, C.; Dimova, R. Mechanical Properties of Plasma Membrane Vesicles Correlate with Lipid Order, Viscosity and Cell Density. *Commun. Biol.* **2019**, 2.

(54) Gracia, R. S.; Bezlyepkina, N.; Knorr, R. L.; Lipowsky, R.; Dimova, R. Effect of Cholesterol on the Rigidity of Saturated and Unsaturated Membranes: Fluctuation and Electrodeformation Analysis of Giant Vesicles. *Soft Matter* **2010**, *6*, 1472−1482.

(55) Merglen, A.; Theander, S.; Rubi, B.; Chaffard, G.; Wollheim, C. B.; Maechler, P. Glucose Sensitivity and Metabolism-Secretion Coupling Studied during Two-Year Continuous Culture in Ins-1e Insulinoma Cells. *Endocrinology* **2004**, *145*, 667−678.

(56) Burns, S. M.; Vetere, A.; Walpita, D.; Dancik, V.; Khodier, C.; Perez, J.; Clemons, P. A.; Wagner, B. K.; Altshuler, D. High-Throughput Luminescent Reporter of Insulin Secretion for Discovering Regulators of Pancreatic Beta-Cell Function. *Cell Metab.* **2015**, *21*, 126−137.

(57) Amatore, C.; Arbault, S.; Bouret, Y.; Guille, M.; Lemaitre, F.; Verchier, Y. Regulation of Exocytosis in Chromaffin Cells by Trans-Insertion of Lysophosphatidylcholine and Arachidonic Acid into the Outer Leaflet of the Cell Membrane. *ChemBioChem* **2006**, *7*, 1998−2003.

(58) Jones, T. t.; Liu, A.; Cui, B. Light-Inducible Generation of Membrane Curvature in Live Cells with Engineered Bar Domain Proteins. *ACS Synth. Biol.* **2020**, *9*, 893−901.

(59) Rossman, J. S.; Jing, X. H.; Leser, G. P.; Lamb, R. A. Influenza Virus M2 Protein Mediates ESCRT-Independent Membrane Scission. *Cell* **2010**, *142*, 902−913.

(60) Martyna, A.; Bahsoun, B.; Badham, M. D.; Srinivasan, S.; Howard, M. J.; Rossman, J. S. Membrane Remodeling by the M2 Amphipathic Helix Drives Influenza Virus Membrane Scission. *Sci. Rep-Uk* **2017**, 7.

(61) Chernomordik, L. V.; Melikyan, G. B.; Chizmadzhev, Y. A. Biomembrane Fusion: A New Concept Derived from Model Studies Using Two Interacting Planar Lipid Bilayers. *Biochim. Biophys. Acta, Rev. Biomembr.* **1987**, *906*, 309−352.

(62) Kozlov, M. M.; Leikin, S. L.; Chernomordik, L. V.; Markin, V. S.; Chizmadzhev, Y. A. Stalk Mechanism of Vesicle Fusion. Intermixing of Aqueous Contents. *Eur. Biophys J.* **1989**, *17*, 121−129.

(63) Stiasny, K.; Heinz, F. X. Effect of Membrane Curvature-Modifying Lipids on Membrane Fusion by Tick-Borne Encephalitis Virus. *J. Virol.* **2004**, *78*, 8536−8542.

(64) Chernomordik, L. V.; Frolov, V. A.; Leikina, E.; Bronk, P.; Zimmerberg, J. The Pathway of Membrane Fusion Catalyzed by Influenza Hemagglutinin: Restriction of Lipids, Hemifusion, and Lipidic Fusion Pore Formation. *J. Cell Biol.* **1998**, *140*, 1369−1382.

(65) Chernomordik, L. V.; Leikina, E.; Frolov, V.; Bronk, P.; Zimmerberg, J. An Early Stage of Membrane Fusion Mediated by the Low PH Conformation of Influenza Hemagglutinin Depends Upon Membrane Lipids. *J. Cell Biol.* **1997**, *136*, 81−93.

(66) Amatore, C.; Bouret, Y.; Travis, E. R.; Wightman, R. M. Interplay between Membrane Dynamics, Diffusion and Swelling Pressure Governs Individual Vesicular Exocytotic Events during Release of Adrenaline by Chromaffin Cells. *Biochimie* **2000**, *82*, 481−496.

(67) Chizmadzhev, Y. A.; Kuzmin, P. I.; Kumenko, D. A.; Zimmerberg, J.; Cohen, F. S. Dynamics of Fusion Pores Connecting Membranes of Different Tensions. *Biophys. J.* **2000**, *78*, 2241−2256.

(68) Hossein, A.; Deserno, M. Spontaneous Curvature, Differential Stress, and Bending Modulus of Asymmetric Lipid Membranes. *Biophys. J.* **2020**, *118*, 91a−91a.

(69) Graber, Z. T.; Shi, Z.; Baumgart, T. Cations Induce Shape Remodeling of Negatively Charged Phospholipid Membranes. *Phys. Chem. Chem. Phys.* **2017**, *19*, 15285−15295.

(70) Doosti, B. A.; Pezeshkian, W.; Bruhn, D. S.; Ipsen, J. H.; Khandelia, H.; Jeffries, G. D. M.; Lobovidna, T. Membrane Tubulation in Lipid Vesicles Triggered by the Local Application of Calcium Ions. *Langmuir* **2017**, *33*, 11010−11017.

(71) Zemel, A.; Ben-Shaul, A.; May, S. Modulation of the Spontaneous Curvature and Bending Rigidity of Lipid Membranes by Interfacially Adsorbed Amphipathic Peptides. *J. Phys. Chem. B* **2008**, *112*, 6988−6996.

(72) Rajendran, L.; Simons, K. Lipid Rafts and Membrane Dynamics. *J. Cell Sci.* **2005**, *118*, 1099−1102.

(73) Yang, S. T.; Kreutzberger, A. J. B.; Kiessling, V.; Ganser-Pornillos, B. K.; White, J. M.; Tamm, L. K. HIV Virions Sense Plasma Membrane Heterogeneity for Cell Entry. *Sci. Adv.* **2017**, 3.

(74) Appourchaux, R.; Delpeuch, M.; Zhong, L.; Burlaud-Gaillard, J.; Tartour, K.; Savidis, G.; Brass, A.; Etienne, L.; Roingeard, P.; Cimarelli, A. Functional Mapping of Regions Involved in the Negative Imprinting of Virion Particle Infectivity and in Target Cell Protection by Interferon-Induced Transmembrane Protein 3 against HIV-1. *J. Virol* **2019**, *93*, No. e01716-18.

(75) Weinberger, A.; Tsai, F. C.; Koenderink, G. H.; Schmidt, T. F.; Itri, R.; Meier, W.; Schmatko, T.; Schroder, A.; Marques, C. Gel-Assisted Formation of Giant Unilamellar Vesicles. *Biophys. J.* **2013**, *105*, 154−164.

(76) Francis, A. C.; Marin, M.; Shi, J.; Aiken, C.; Melikyan, G. B. Time-Resolved Imaging of Single HIV-1 Uncoating *in Vitro* and in Living Cells. *PLoS Pathog.* **2016**, *12*, No. e1005709.

Interferon-Induced Transmembrane Protein 3 Blocks Fusion of Diverse Enveloped Viruses by Altering Mechanical Properties of Cell Membranes

Xiangyang Guo, Jan Steinkühler, Mariana Marin, Xiang Li, Wuyuan Lu, Rumiana Dimova and Gregory B. Melikyan

**Supplementary Figures, Figure Legends, Movie Legend and Appendix**
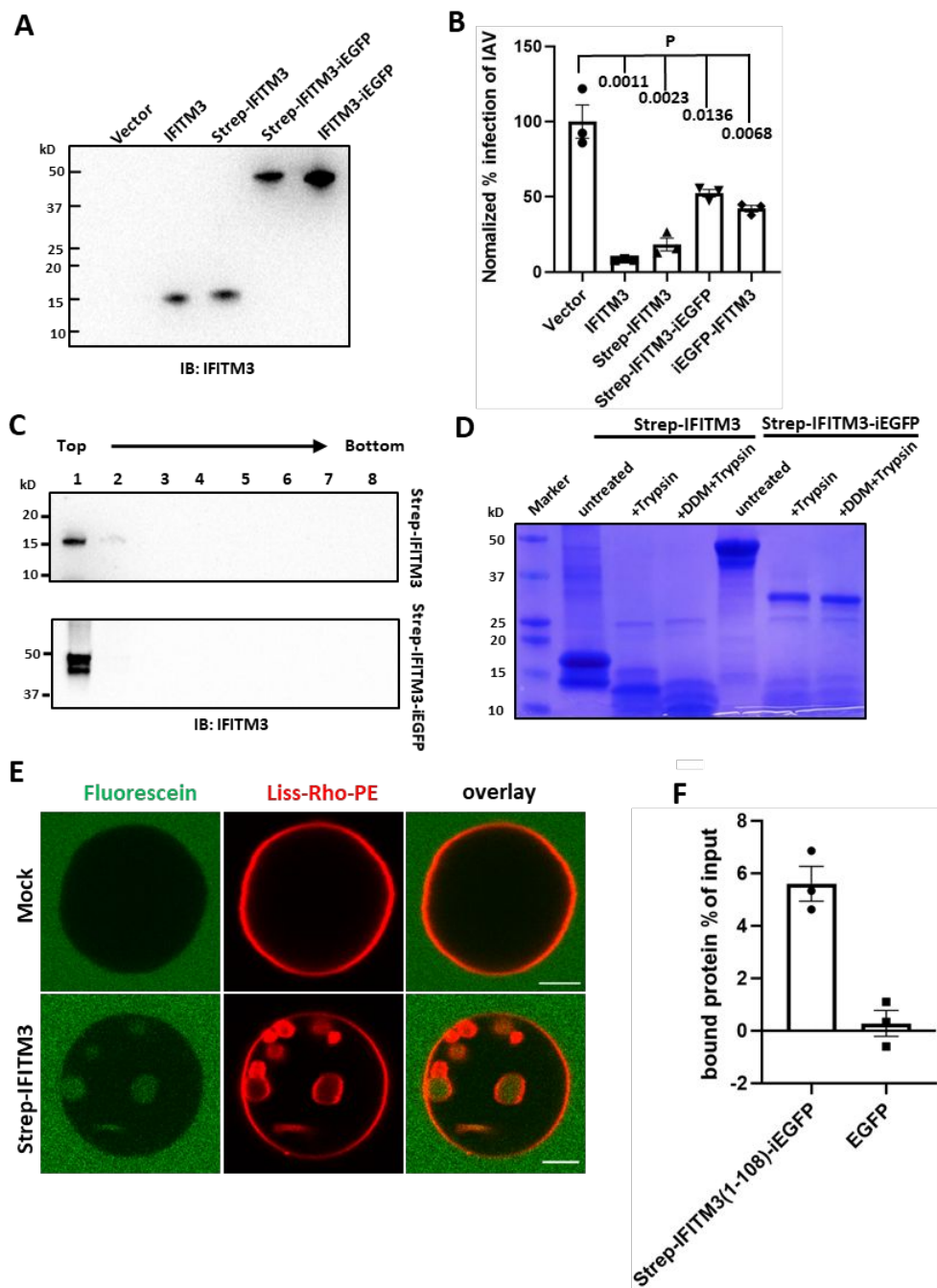
Figure S1. IFITM3 induces negative membrane curvature *in vitro*. (A) Expression levels of different IFITM3 constructs in transfected HEK 293T/17. HEK 293T/17 cells transfected with an empty Vector, unlabeled IFITM3, Strep-IFITM3, IFITM3-iEGFP, or Strep- IFITM3-iEGFP were lysed and analyzed by Western blotting using a rabbit antibody against the N-terminal region of IFITM3. (B) IAV pseudovirus infection is inhibited in HEK 293T/17 cells expressing IFITM3 constructs described in (A). The extent of infection by IAV pseudovirus carrying the luciferase gene measured by

luciferase activity is shown as a percentage of infection in cells transfected with empty vector. Data represent mean ± SEM (n = 3). (C) Strep-IFITM3 and Strep-IFITM3-iEGFP-reconstituted LUVs were subjected to floatation analysis. After density gradient centrifugation, collected fractions were analyzed by SDS–PAGE and Western blotting using rabbit anti-IFITM3 antibody. (D) Strep-IFITM3- and Strep-IFITM3-iEGFP-reconstituted LUVs were incubated with trypsin at 37 °C for 30 min. As a control, 0.2% n-Dodecyl-B-D-maltoside (DDM) was added with trypsin to permeabilize LUV membrane. The samples were analyzed by SDS-PAGE and stained with Coomassie blue. (E) Fluorescein (0.3 μM) was added to the external buffer of GUVs prepared from mock-treated LUVs (top) and from Strep-IFITM3-reconstituted LUVs (bottom) immediately after electroformation to mark *bona fide* inward budding events in GUVs. Scale bars 10 μm. (F) Membrane binding of Strep-IFITM3(1-108)-iEGFP assessed by a liposome co-sedimentation assay. Two mM of LUVs (99.0 mol % POPC, 0.5 mol % cholesterol, 0.5 mol % Liss-Rho-PE) were incubated at room temperature with 1 μM Strep-IFITM3(1-108)-iEGFP or EGFP for 10 min and then spun down by ultra-centrifugation. The bound % of protein was deduced from the reduction of EGFP fluorescence in supernatant and normalized by comparing with the fluorescence of input samples. Data represent mean ± SEM of the results of three independent experiments.

3
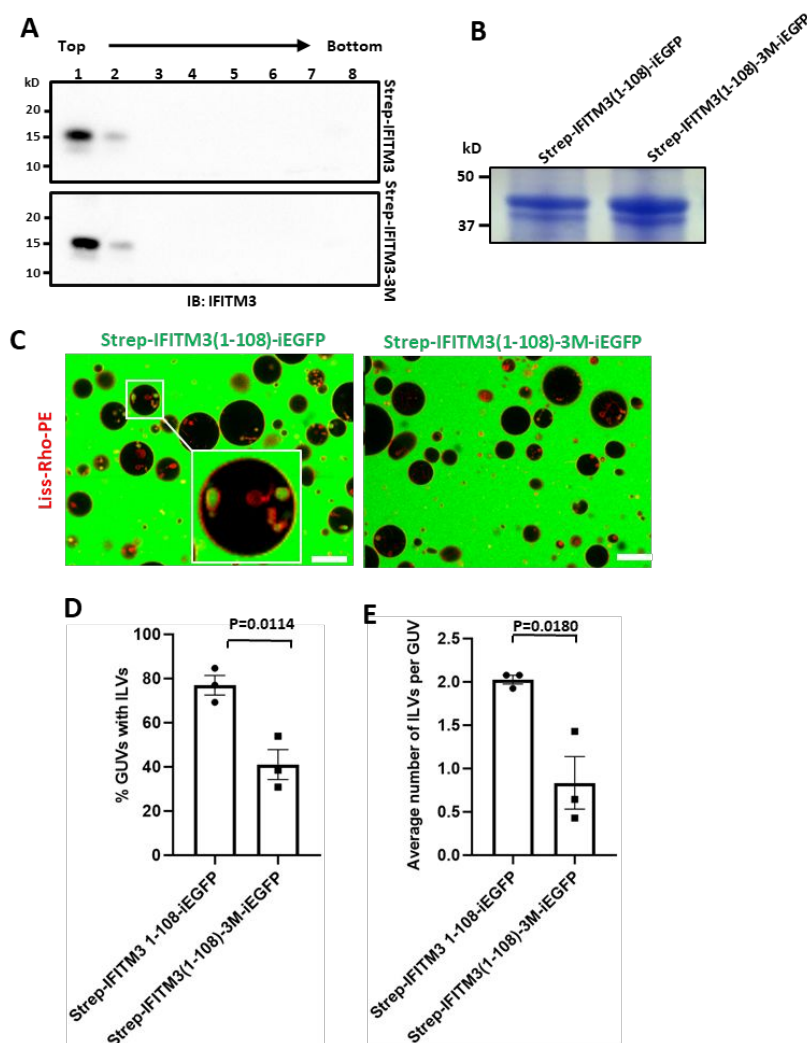
Figure S2. IFITM3 amphipathic helix is responsible for induction of negative membrane curvature. (A) Strep-IFITM3- and Strep-IFITM3-3M-reconstituted LUVs were subjected to floatation analysis. After density gradient centrifugation, collected fractions were analyzed by SDS–PAGE and Western blotting using rabbit anti-IFITM3 antibody. (B) Coomassie blue staining of purified Strep-IFITM3(1-108)-iEGFP and Strep-IFITM3(1-108)-3M-iEGFP. (C) GUVs (red) were incubated with 20 μM Strep-IFITM3(1-108)-iEGFP or Strep-IFITM3(1-108)-3M-iEGFP (green) for 30 min and imaged. Scale bars 10 μm. (D) Quantification of inward budding showing the percentage of GUVs, prepared and treated as in (C), with at least one intraluminal vesicle (ILV) containing EGFP. Data represent mean ± SEM of the results of three independent experiments, with 13 GUVs analyzed per sample in each experiment. (E) As in (D), but the plots represent the average number of ILVs per GUV.
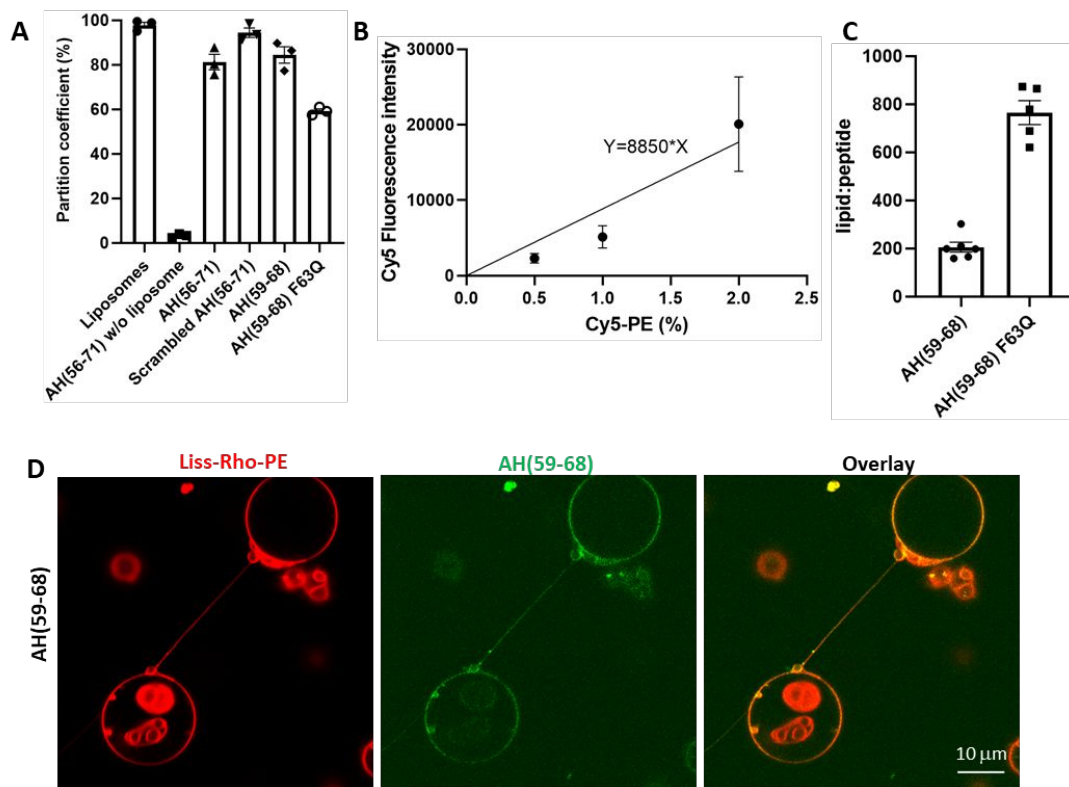
Figure S3. Membrane binding activity analysis of IFITM3 AH. (A) Partition coefficients of peptides. Two mM of LUVs (99.0 mol % POPC, 0.5 mol % cholesterol, 0.5 mol % Liss-Rho-PE) were incubated at room temperature with 40 μM of Cy5-labeled peptides for 10 min and spun down by ultra-centrifugation. The partition coefficient of peptides was deduced from reduction of Cy5 fluorescence in supernatant and normalized to the fluorescence input and is represented as % bound peptide relative to the input. Data represent mean ± SEM of the results of two independent experiments. Liposomes represents no-peptide control. (B) A standard curve of fluorescence intensity for varied concentrations of Cy5-PE incorporated in GUV membranes. Fluorescence intensity was analyzed by ImageJ using the Radial Profile Angle plugin. (C) Surface density of IFITM3 AH(59-68) and AH(59-68)F63Q on the GUV membrane was calculated by comparing the fluorescence intensity of the Cy5-conjugated AH with the standard curve in (B). (D) GUV tube-pulling assay was used to generate positively curved nanotubes. The AH(59-68) peptide (10 μM) was added after tube formation.
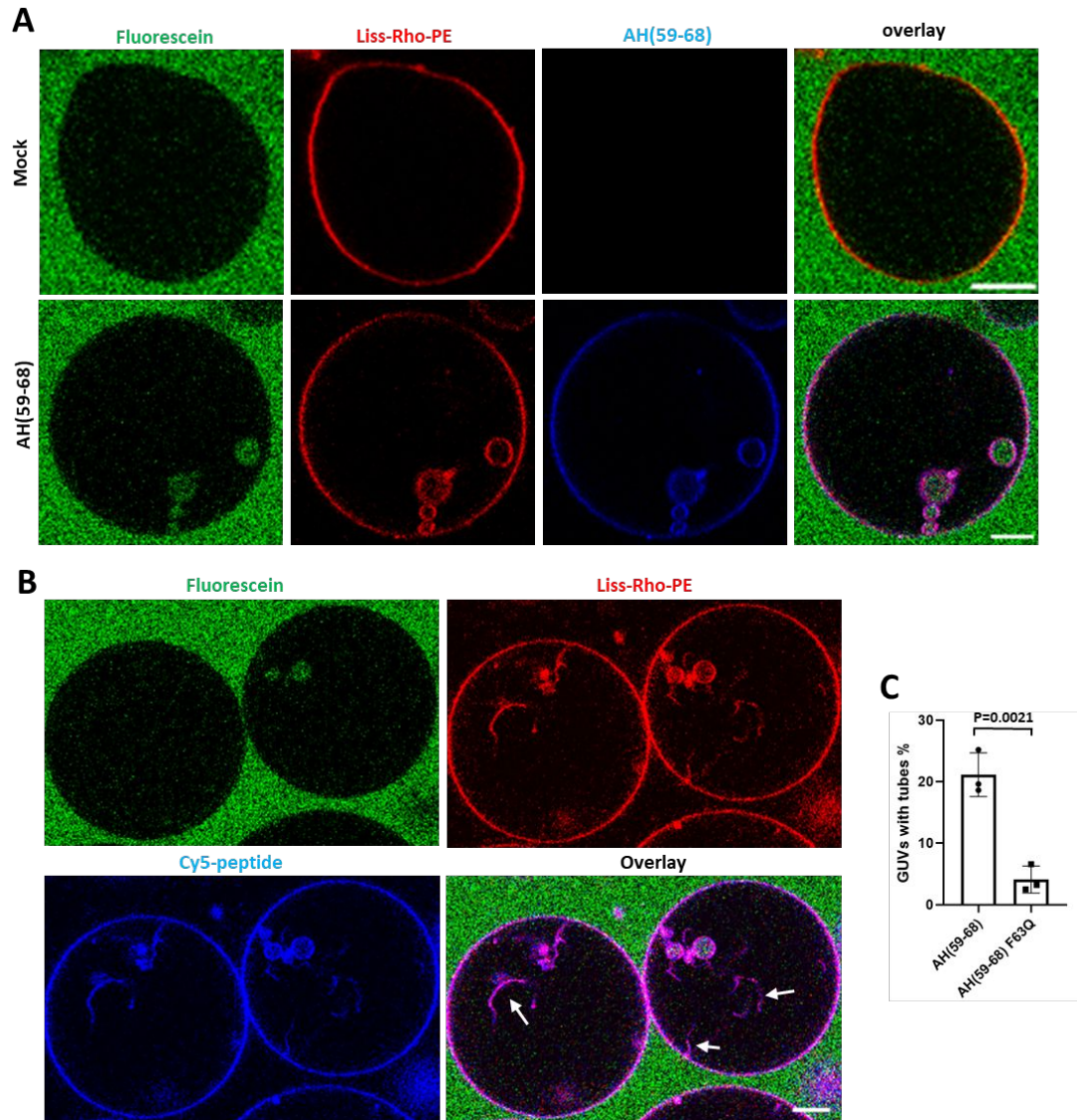
Figure S4. IFITM3 AH is sufficient to induce the formation of ILVs and nanotubes in GUVs. (A) GUVs prepared from a liver polar extract were treated with 10 μM AH(59-68) (bottom) or the same volume of DMSO (mock, top) for 30 min and imaged. Fluorescein (0.3 μM) was added to the external buffer to mark inward budding of GUVs occurring after electroformation. Scale bars 5 μm. (B) GUVs were treated with 10 μM AH(59-68) for 30 min and imaged. Fluorescein (0.3 μM) was added to the external buffer to mark inward budding of GUVs occurring after electroformation. Arrows indicate nanotubes. Scale bars 10 μm. (C) Percentage of GUVs, treated with 10 μM AH(59-68) or 10 μM AH(59-68)F63Q, with at least one nanotube that has AH-conjugated Cy5 fluorescence. Data represent mean ± SEM of the results of three independent experiments.
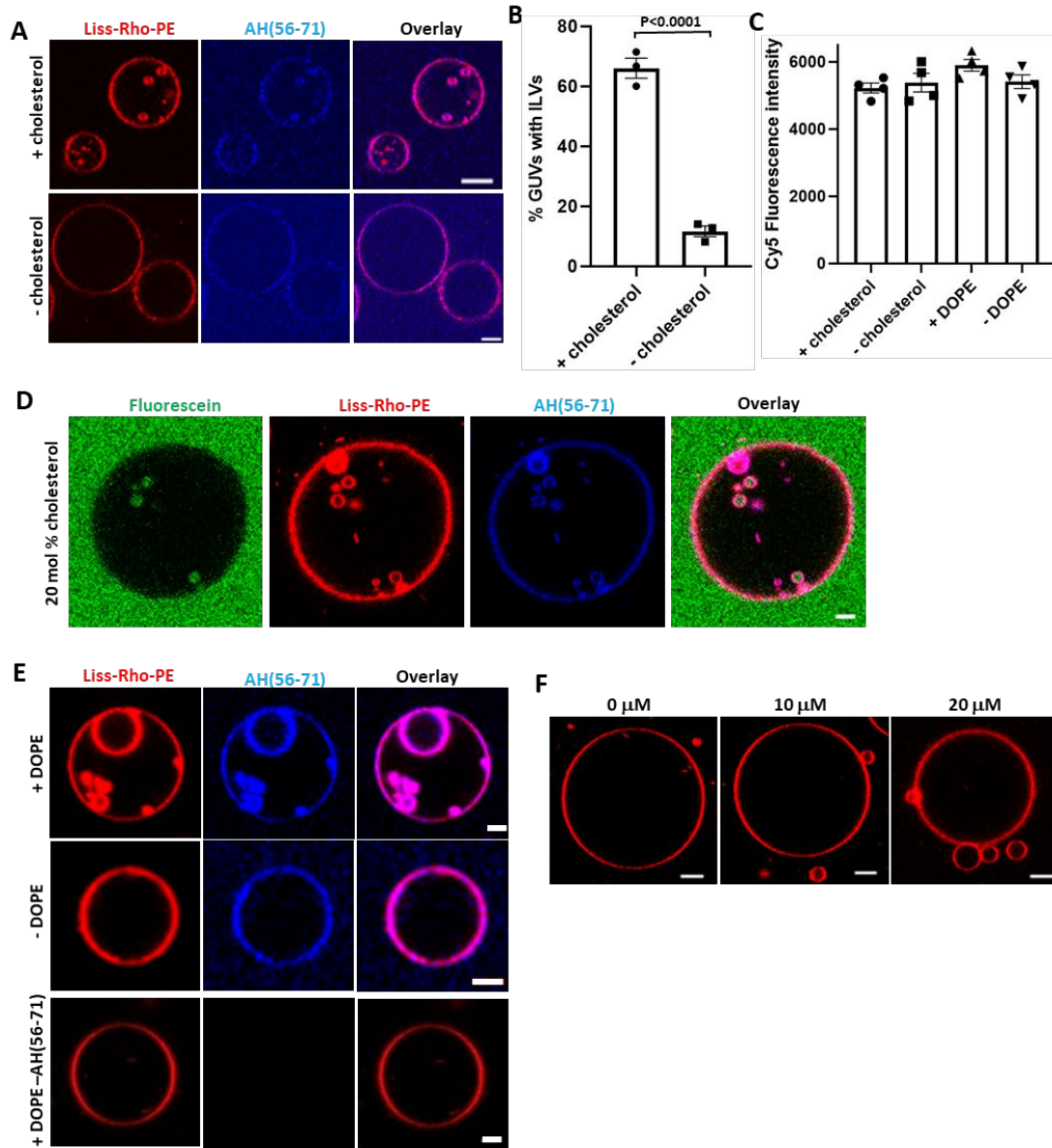
Figure S5. Negative membrane curvature induced by IFITM3 is facilitated by cholesterol, POPE and counteracted by lyso-lipids. (A) GUVs with cholesterol (99.0 mol % POPC, 0.5 mol % cholesterol, 0.5 mol % Liss-Rho-PE) or GUVs without cholesterol (99.5 mol % POPC, 0.5 mol % Liss-Rho-PE) were incubated with 10 μM AH(56-71) for 30 min and imaged. Scale bars 10 μm. (B) Quantification of inward budding showing the percentage of GUVs, prepared and treated as in (A), with at least one intraluminal vesicle (ILV) containing Cy5-labeled peptide. Data represent mean ± SEM of three independent experiments, with 45 GUVs analyzed per sample in each experiment. (C) Fluorescence intensity of Cy5-labeled AH(59-68) on the surface of GUVs ± cholesterol or GUVs ± DOPE, measured using the ImageJ Radial Profile

7

Angle plugin. (D) GUVs (79.5 mol % POPC, 20 mol % cholesterol, 0.5 mol % Liss-Rho-PE) were incubated with 10 μM AH(56-71) for 30 min and imaged. Scale bars 5 μm. (E) GUVs without POPE (99.0 mol % POPC, 0.5 mol % cholesterol, 0.5 mol % Liss-Rho-PE) or with POPE (79.5 mol % POPC, 20 mol % DOPE, 0.5 mol % Liss-Rho-PE) were incubated with 10 μM AH(56-71) for 30 min and imaged. Scale bars 5 μm. (F) GUVs (99.0 mol % POPC, 0.5 mol % cholesterol, 0.5 mol % Liss-Rho-PE) were treated with an indicated concentration of LPC for 30 min and imaged. Scale bars 10 μm.
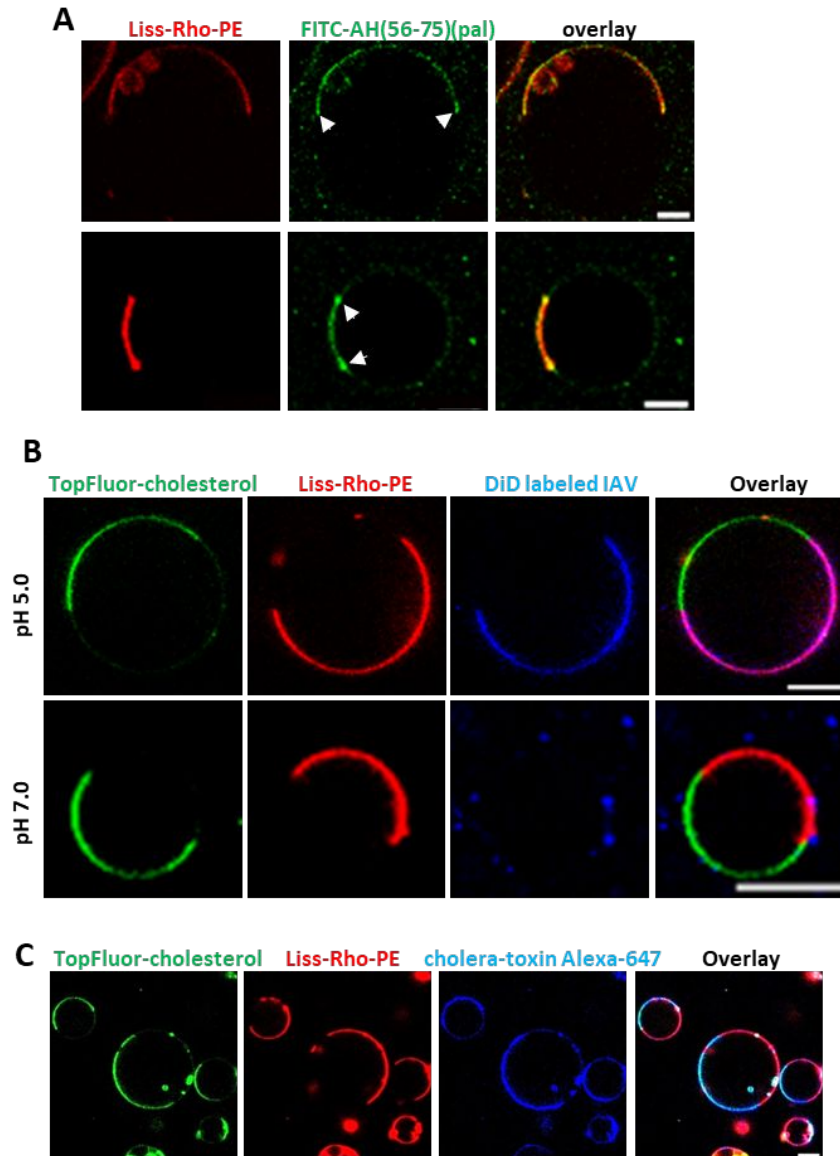
Figure S6. IFITM3 partitions into liquid-disordered membrane domains that support IAV fusion. (A) Shown are two examples of phase-separated GUVs (33.3 mol % DOPC, 33.3 mol % SM, 32.4 mol % cholesterol, 0.5 mol % TopFluor-cholesterol and 0.5% Liss-Rho-PE) incubated with 10 μM of FITC-labeled palmitoylated AH (FITC-AH(56-75)(pal)) for 30 min. Arrows indicate accumulation of FITC-AH(56-75)(pal) peptide at the phase boundary. Scale bars 5 μm. (B) Phase-separated GUVs (33.3 mol % DOPC, 33.3 mol % SM, 30.4 mol % cholesterol, 2% GM1, 0.5 mol % TopFluor-cholesterol and 0.5% Liss-Rho-PE) were mixed with DiD-labeled IAV. Lipids mixing between IAV and GUV was triggered by addition of a predetermined amount of citrate buffer to achieve the final pH of 5.0 and samples were immediately imaged. PBS (pH 7.2) was used as control. Scale bars 10 μm. (C) GM1 in phase-

separated GUVs (33.3 mol % DOPC, 33.3 mol % SM, 30.4 mol % cholesterol, 2% GM1, 0.5 mol % TopFluor-cholesterol and 0.5% Liss-Rho-PE) was stained with cholera-toxin B Alexa-647. Scale bars 10 μm.
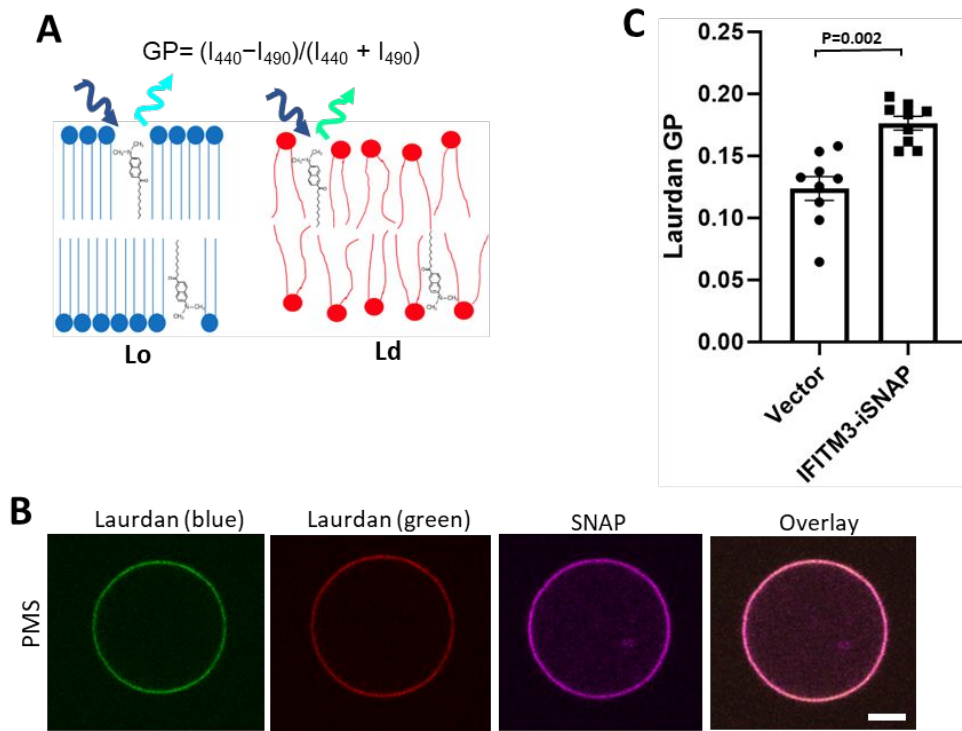
Figure S7. Full-length IFITM3 increases lipid order. (A) A diagram illustrating the principle of Laurdan-based measurements of lipid order. (B) Plasma membrane spheres were prepared from IFITM3-iSNAP expressing A549 cells by cell swelling and stained with SNAP-cell 647-SIR (violet) for SNAP and treated with Laurdan for lipid order measurement. The Laurdan fluorescence signal was acquired from 419 nm to 464 nm for the blue channel and from 472 nm to 517 nm for the green channel. Scale bars 10 μm. (C) General Polarization (GP) of Laurdan was calculated using the equation $GP = (I_b - I_g)/(I_b + I_g)$ (I_b and I_g represent Laurdan fluorescence from the blue channel and the green channel, respectively) based on the ratio of Laurdan fluorescence of plasma membrane spheres prepared from IFITM3-iSNAP expressing A549 cells and cells transduced with empty vector (control). Data represent mean ± SEM of at least three independent experiments.
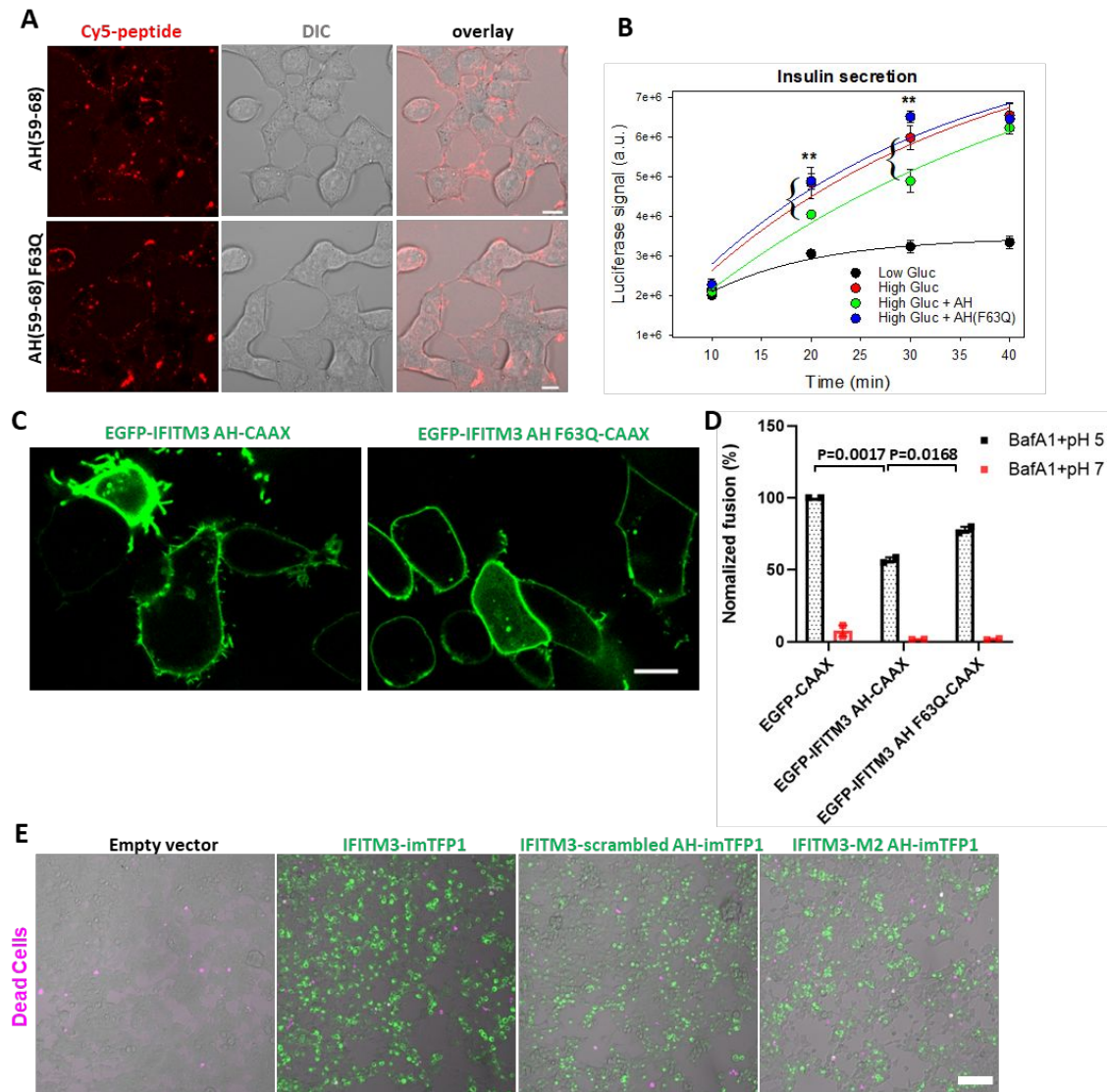
Figure S8. IFITM3 AH is sufficient to inhibit membrane fusion. (A) INS-1E cells were treated with 5 µM AH(59-68) or 10 µM AH(59-68)F63Q for 5 min and imaged. Scale bars 10 µm. (B) Time course of glucose-stimulated insulin secretion in INS-1E cells transduced with proinsulin-luciferase fusion construct. INS-1E cells were preincubated for 5 min with 5 µM AH(59-68) or 10 µM AH(59-68)F63Q and stimulated for 20 min with a high glucose (20 mM, HG) or low glucose (2.8 mM, LG) buffer as control. Luciferase activity was measured for each time point by adding the coelenterazine substrate to the supernatant and reading on a Luminescence counter. Data represent mean ± SD of the results of two independent experiments. **, $p < 0.01$ for HG and HG + AH(59-68) samples. (C) 293T cells expressing EGFP-IFITM3 AH-CAAX or EGFP-IFITM3 AH F63Q-CAAX (green). Scale bar 10 µm. (D) Forced

fusion of IAV/BlaM-Vpr pseudoviruses at the plasma membrane of A549 cells expressing either EGFP-CAAX, or EGFP-IFITM3 AH-CAAX or EGFP-IFITM3 AH F63Q-CAAX. Fusion of cell-bound viruses was induced by exposure to a pH 5.0 buffer, as described in Methods. Data represent mean ± SEM of two independent experiments, each in triplicates. (E) HEK 293T/17 cells expressing wild-type or scrambled imTFP1-tagged IFITM3 or IFITM3 M2 AH chimera were infected by IAV and cell viability was tested using a LIVE/DEAD™ Fixable Far Red Dead Cell Stain Kit 12 h after infection. Dead cells are shown in magenta. Scale bar 100 μm.

Supplemental Table 1. Key resources.

REAGENT or RESOURCE	SOURCE	IDENTIFIER
Antibodies		
Rabbit anti IFITM3 (N-term) antibody	Abgent	AP1153a
Bacterial and Virus Strains		
Rosetta™ 2 (DE3) pLysS Singles™	MilliporeSigma	Cat#71401-M
NEB® 5-alpha Competent E. coli	New England Biolabs	Cat#C2987H
Influenza A/PR/8/34(HIN1)	Charles River Laboratories	Cat#10100374
PR8-mCherry H1N1 IAV	PMID: 28798254	N/A
Chemicals, Peptides, and Recombinant Proteins		
Streptavidin, Alexa Fluor™ 647 conjugate	Thermo Fisher Scientific	Cat#S21374
Streptavidin	Thermo Fisher Scientific	Cat#PI21125
BSA-Biotin	Thermo Fisher science	Cat#29130
Cholera Toxin Subunit B (Recombinant), Alexa Fluor 647	Thermo Fisher Scientific	Cat#C34778
ANAPOE-X-100	Anatrace	Cat#APX100
BioBeads SM-2 absorbent beads	Bio-Rad	Cat#1528920
POPC	Avanti Polar Lipids	Cat#850457
DOPC	Avanti Polar Lipids	Cat#850375
DOPE	Avanti Polar Lipids	Cat#850725
18:1 Biotinyl Cap PE	Avanti Polar Lipids	Cat#870273
18:0 Lyso PC	Avanti Polar Lipids	Cat#855775
18:0 SM	Avanti Polar Lipids	Cat#860586
cholesterol (ovine)	Avanti Polar Lipids	Cat#700000
Ganglioside GM1 (Ovine Brain)	Avanti Polar Lipids	Cat#860065
TopFluor® Cholesterol	Avanti Polar Lipids	Cat#810255
Liver Extract Polar	Avanti Polar Lipids	Cat#181108
DiD solid	Thermo Fisher Scientific	Cat#D7757
cOmplete EDTA-free Protease Inhibitor Cocktail	Roche	Cat#11873580001
Bafilomycin A1	Sigma	Cat#B1793-10UG
Rabbit anti IFITM3 (N-term) antibody	Abgent	AP1153a
Strep-Tactin Superflow Plus	Qiagen	Cat#30004
CCF4-AM	Invitrogen	Cat#K1095
Experimental Models: Cell Lines		
HEK293T/17	ATCC	ACS-4500
A549	ATCC	CCL-185
INS-1E	Addexbio Technologies	Cat#C0018009
Recombinant DNA		
pQCXIP	Takara Bio USA, Inc.	Cat#631515
Proinsulin-NanoLuc	Addgene PMID: 25565210	Cat#62057
psPAX2	Addgene	Cat#12260
pMD2.G	Addgene	Cat#12259
pCAGGS HA WSN/33	PMID: 22046135	N/A
pCAGGS NA WSN/33	PMID: 22046135	N/A
pNL4-3.Luc.R–E–	NIH AIDS Reagent Program	Cat#3418
pcRev	NIH AIDS Reagent Program	Cat#11415

pR9ΔEnv	15	PMID: 29649444	
Software and Algorithms			
Fiji/ImageJ		https://imagej.nih.gov/ij/docs/guide/146-2.html	RRID:SCR_002285
Graphpad		https:www.graphpad.com/	N/A

Supplemental Video S1. 3D image series of GUVs containing ILVs and nanotubes. Movie shows z-stacks of a Strep-IFITM3-iEGFP (green)-reconstituted GUV (labeled with Liss-Rho-PE, red) scanned from bottom to top with a z-section interval of 0.2 μm. Scale bar 10 μm.

Supplemental Appendix

AH(59-68) was observed to induce nanotubes (cylindrical or neckless-like structures of high curvature below the optical resolution) in the GUV lumen (Figs. 2B and S4B, movie S1). This observation was used to obtain an order-of-magnitude estimate of the membrane curvature generated by the AH(59-68) peptide. This estimate was then compared to other membrane curvature inducing proteins.

The widely used curvature elasticity model implies a membrane spontaneous curvature of $m = -c * 1/R_{tube}$ with a pre-factor c of 1/2 or 1 for homogenous lipid bilayers that form GUVs with coexisting inward-pointing nanotubes.[1] As in our experiments the exact radius R_{tube} of the tubes cannot be resolved, we take the optical resolution limit (250 nm) as an upper limit for the tube diameter $2*R_{tube}$. By taking c=1/2, we obtain a lower limit for the spontaneous curvature generated by AH(59-68).[2] In the dilute regime, where peptide-peptide interactions are neglectable, one can consider the curvature generated per peptide as $m = \phi * m_0$, where ϕ is the membrane area fraction occupied by the peptide. To estimate ϕ from fluorescence measurements showing that 1 peptide is bound per 100 lipid molecules of the external leaflet of GUV (Fig. S3B, C), we approximated the footprint of the alpha-helical peptide on the membrane as a flat cylinder at the lipid-water interface (1.8 nm²) and assumed 0.7 nm² for area per lipid molecule.

We find $m_0^{-1} \approx -6.4$ nm, which is comparable to the membrane curvature generated by amphiphysin 1 in the dilute regime.[3] However, while AH(59-68) induces negative curvature, amphiphysin 1 generates positive curvature. Thus, the effect of AH(59-68) might be better compared to I-BAR protein, which was also found to have a similar value of m_0 of same sign.[4] Compared to the literature values, our estimate is based only on a single protein density and has larger uncertainties. However, as the calculations varies only linearly in respect to the experimental uncertainties, we remain confident about the order of magnitude for our estimate of m_0.

We note that the estimate for m_0^{-1} is comparable to the bilayer thickness, which is the relevant length-scale for bilayer stalk formation and fusion. In summary, we conclude that the local ("intrinsic") curvature generated by AH(59-68) is rather large, comparable to that for established physiological curvature-inducing proteins. This curvature should have a major contribution to the energetics of membrane remodeling, even at dilute concentrations and on smaller scales than is directly observable in the GUV experiments.

REFERENCES

(1) Li, Y. H.; Lipowsky, R.; Dimova, R., Membrane Nanotubes Induced by Aqueous Phase Separation and Stabilized by Spontaneous Curvature. *P Natl Acad Sci USA* **2011,** *108*, 4731-4736.

(2) Steinkuhler, J.; Knorr, R. L.; Zhao, Z. L.; Bhatia, T.; Bartelt, S. M.; Wegner, S.; Dimova, R.; Lipowsky, R., Controlled Division of Cell-Sized Vesicles by Low Densities of Membrane-Bound Proteins. *Nature Communications* **2020,** *11*.

(3) Sorre, B.; Callan-Jones, A.; Manzi, J.; Goud, B.; Prost, J.; Bassereau, P.; Roux, A., Nature of Curvature Coupling of Amphiphysin with Membranes Depends on Its Bound Density. *P Natl Acad Sci USA* **2012,** *109*, 173-178.

(4) Chen, Z.; Shi, Z.; Baumgart, T., Regulation of Membrane-Shape Transitions Induced by I-BAR Domains. *Biophys J* **2015,** *109*, 298-307.